Density Functional Theory Modeling of the Oxidation Mechanism of Co(II) by Birnessite

Alain Manceau, Stephan N Steinmann

DFT Modeling of the Oxidation Mechanism of Co(II) by Birnessite

Alain Manceau[*a] and Stephan N. Steinmann[b]

[a] Univ. Grenoble Alpes, Univ. Savoie Mont Blanc, CNRS, IRD, ISTerre, 38000 Grenoble, France

[b] ENS de Lyon, CNRS, Laboratoire de Chimie, 69342 Lyon, France

Corresponding Author :

alain.manceau@univ-grenoble-alpes.fr

Keywords: Phyllomanganate, cobalt, manganese, nickel, comproportionation

ABSTRACT

Phyllomanganates of the birnessite family are the most abundant manganese oxides on Earth and the strongest inorganic oxidants in the environment. Birnessite controls the oxidative scavenging of cobalt in soils, lake and marine sediments, and ferromanganese crusts and nodules, leading to enrichments of the order of one billion times the concentration in solution. However, a detailed mechanistic understanding of the enrichment processes is lacking. Here, we perform density functional theory (DFT) calculations to explore the mechanisms of Co(II) to Co(III) oxidation on the layer edge and surface of birnessite nanoparticles. We show that Co(II) sorption on a layer edge is an unlikely oxidation pathway. In contrast, Co(II) sorbed on a Mn(IV) vacancy site exposed on the layer surface as an octahedral triple-corner sharing (TCS) complex enters the vacancy where it is oxidized to Co(III) by a layer Mn(IV) cation, which is reduced to Mn(III). The stepwise reaction proceeds as follows. The octahedral TCS complex is transformed to a smaller tetrahedral TCS complex, allowing Co(II) to cross the surface oxygen layer and to fill the empty octahedral Mn(IV) site. When in the octahedral vacancy, Co(II) is converted from the high-spin ($t_{2g}^5e_g^2$) to the low-spin ($t_{2g}^6e_g^1$) state and the Co(II) octahedron becomes strongly distorted by the Jahn-Teller effect. Afterward, the electron exchange reaction between Mn(IV) ($t_{2g}^3e_g^0$) and Co(II) ($t_{2g}^6e_g^1$) takes place, resulting in the formation of a regular low-spin Co(III) ($t_{2g}^6e_g^0$) octahedron and a Jahn-Teller distorted high-spin Mn(III) ($t_{2g}^3e_g^1$) octahedron. These findings refine previously proposed mechanisms of Co(II) oxidation by birnessite and fill gaps in our understanding of global Co sequestration in natural systems.

1. INTRODUCTION

Manganese dioxides (MnO_2) dominate the geochemistry of cobalt (Co) in terrestrial and marine environments.[1–22] For example, the partitioning of Co between seawater and marine ferromanganese crusts is as high as 10^9, and the second highest of all chemical elements after lead (Pb).[23] Evidences for the strong uptake of Co by MnO_2 has aroused the interest of scientists for decades and led to multiple sorption and coprecipitation studies aimed to understand the underlying chemical reaction on abiotic and biogenic MnO_2,[24–29] and the structure, reactivity, and stability of Co-containing MnO_2.[30–33]

Early observations of the Co-MnO_2 geochemical association in the 1970s invoked the oxidation of soluble Co(II) to insoluble Co(III) by Mn oxide minerals,[34–36] and first direct evidences were obtained in 1979-1983 by Murray, Dillard, and Crowther using XPS.[37–39] Mn(IV) was identified as the oxidizing agent at pH 6.5 based on the detection of Mn(III) in the birnessite phyllomanganate reacted with Co(II) under anaerobic condition. The XPS analysis was revisited by Yin et al.[28] in 2011. This time, the authors measured the fractions of Mn(IV), Mn(III), and Mn(II) before and after Co(II) sorption on birnessite at pH 5, and observed an increase of both Mn(III) and Mn(II) on the solid phase. They confirmed that Mn(IV) was the primary oxidant and explained the occurrence of Mn(II) by the disproportionation of two reduced Mn(III) cations into Mn(IV) + Mn(II).

Burns[35] conjectured in 1976 that the edge-shared [MnO_6] octahedral layers of birnessite contained Mn(IV) vacancies like chalcophanite,[40,41] and that Co(III) filled the vacated Mn(IV) sites on the basis of crystal field stabilization energies (CFSE) and steric considerations. Progress on the oxidation mechanism of Co(II) remained at a standstill for the following two decades due to the lack of robust structural model for birnessite. In 1997, Drits et al. [42,43] synthesized and determined the structure of well-crystallized hexagonal birnessite (HBi) using electron and X-ray diffraction and chemical analysis. Ever since, nanoparticulate hexagonal birnessite (δ-MnO_2) has been identified in soils, lake and marine sediments, and mineral surface coatings and rock varnish, and is the main MnO_2 species produced by bacteria and fungi.[44–51] It is recognized to be the most abundant MnO_2 species at the Earth's surface.[6,9,11,20,52–73]

The elemental composition of HBi is non-stoichiometric and has for generic formula $H_x^+Mn_y^{3+}Mn_z^{2+}(Mn_u^{4+}Mn_v^{3+}\square_w)O_2$,[74] in which □ denotes an empty Mn(IV) position. The -4 charge deficit created by a vacancy is balanced by two H^+ on each side of the MnO_2 layer. Using EXAFS spectroscopy, Silvester et al.[43] found in 1997 that the two protons on one side of a vacancy could be displaced by Zn(II) at pH 4 to form an interlayer triple-corner-sharing (TCS) inner-sphere complex at the surface of the MnO_2 layers (Figure 1a). The same year, Manceau et al.[75] described the incorporation

at pH 4 of Co(III) into the octahedral vacancies (incorporated INC complex), consecutively to the oxidation of a Co^{2+}_{TCS} complex (Figure 1b). Mn(III) was inferred to be the electron acceptor because Mn(III) is considered to be a stronger oxidant than Mn(IV).[75–77]

Two reaction mechanisms were proposed based on X-ray diffraction, and powder and polarized EXAFS spectroscopy. The first mechanism can be written

$$Co^{2+}_{Sol} + \square_1 + Mn^{3+}_{Layer} \rightarrow Co^{2+}_{TCS} + \square_1 + Mn^{3+}_{Layer} \rightarrow Co^{3+}_{TCS} + \square_1 + Mn^{2+}_{Layer} \rightarrow Co^{3+}_{INC} + \square_2 + Mn^{2+}_{TCS/Sol} \quad (1)$$

where a solution (sol) Co(II) cation is sorbed on an existing vacancy, is oxidized by a layer Mn(III) cation, and the reduced Mn(II) cation either migrates to the interlayer forming a Mn^{2+}_{TCS} complex (TCS), or to solution creating a new vacancy. This mechanism can lead to high Co(III) enrichment because the density of vacancies remains constant. The second mechanism can be written

$$Co^{2+}_{Sol} + Mn^{3+}_{TCS} + \square \rightarrow Mn^{2+}_{Sol} + Co^{3+}_{TCS} + \square \rightarrow Mn^{2+}_{Sol} + Co^{3+}_{INC} \quad (2)$$

where a Co(II) cation undergoes oxidation by an interlayer Mn(III) cation, which is released to solution. This reaction mechanism decreases the density of vacancies, and therefore diminishes the surface reactivity of birnessite over time.

In 2012, Yu et al.[78] sorbed Co(II) on abiotic and biogenic birnessite of different crystallinity and with various proportions of interlayer Mn(III). They found using EXAFS spectroscopy and elemental analysis that Co(II) was oxidized by Mn^{3+}_{TCS}, which was reduced to Mn(II) in nearly equimolar Co(III):Mn(II) ratio. In 2015, Simanova and Peña[26] used quick XANES and EXAFS spectroscopy to compare the reactivity of the basal and lateral surface sites of δ-MnO_2.[79,80] Two main Co-Mn EXAFS distances were measured, 2.83-2.86 Å attributed to a Co(III)-Mn edge-sharing (ES) octahedral linkage, and 3.47-3.50 Å attributed to a Co(II)-Mn corner-sharing (CS) octahedral linkage. When the ES [CoO_6] octahedron is located inside the MnO_2 layer (INC complex), the number of nearest Mn neighbors is six, and when it is located at the nanoparticle edges, it is two for a double-edge sharing complex (DES) and three for a triple-edge sharing complex (TES, Figures 1b-d). A CS [CoO_6] octahedron has six nearest Mn neighbors in TCS position (Figure 1a), and two in double-corner-sharing (DCS) position at the nanoparticle edges (Figure 1e). EXAFS coordination numbers (CNs) are the weighted mean of the coordination numbers of all atoms bonded to δ-MnO_2. Therefore, the distribution of Co between the INC and DES sites can be inferred in principle from the CNs of the nearest Co-Mn_1 shell at 2.83-2.86 Å (ES linkage), and the distribution of Co between the DCS and TCS sites can be inferred from the CNs of the next-nearest Co-Mn_2 shell at 3.47-3.50 Å (CS linkage). Low CNs will reflect preferential

adsorption on lateral surfaces as DES and DCS complex, whereas high CNs will reflect preferential adsorption on basal surfaces as TCS and INC complex.

Simanova and Peña[26] observed in 2015 that CN(ES) increased from 3.12 ± 0.49 after 7 min to 4.13 ± 0.62 after 12 h reaction time at low surface coverage (Co/Mn = 0.05). CN(CS) increased in parallel from 2.71 ± 0.43 to 5.39 ± 1.76. This evolution was interpreted to indicate that Co(II) is oxidized more rapidly on lateral than on basal surfaces. The fast oxidation on lateral surfaces was described as follows:

$$Co^{2+}_{Sol} + Mn^{3+}_{Layer} \rightarrow Co^{2+}_{DCS} + Mn^{3+}_{Layer} \rightarrow Co^{3+}_{Layer} + Mn^{2+}_{Sol} \quad (3)$$

where a solution Co(II) sorbs as a DCS complex, is oxidized to Co(III) by a Mn^{3+}_{Layer} cation, and takes its position on the layer edge while Mn(III) is reduced to Mn^{2+}_{Sol}. TES complexation of Co(II) was not considered, and is unlikely to occur, because a TES surface site would have a high interfacial excess energy and would be immediately filled with a Mn(IV) cation to minimize the Gibbs free energy of the MnO_2 layer. The slow oxidation reaction was attributed to reaction 2 of Manceau et al.[75] The slow kinetics was explained by the lack of bridging ligand between the hexahydrated Co^{2+}_{sol} ion and the Mn^{3+}_{TCS} octahedron, and the outer-sphere mechanism of the electron transfer thereof. Wang et al.[29] pursued in 2018 the study of Simanova and Peña[26] and concluded that the kinetics of oxidation on vacancy sites is also limited by diffusion process in the interlayer space of the δ-MnO_2 nanosheets.

Density functional theory (DFT) modeling of Ni(II), Cu(II), and Zn(II) uptake by birnessite predicts that sorption as DES complex is favored over sorption as DCS and TCS complex,[81] which is consistent with free edge-shared surface sites being the crystal growth sites of two-dimensional compounds. Therefore, formation of a Co^{2+}_{DCS} complex (reaction 3) challenges current understanding of the surface reactivity of birnessite.

Here, a DFT modeling of the oxidation mechanism of Co(II) on birnessite was conducted to explore the oxidation pathways of Co(II) on the lateral and basal surface sites, and whether the electron acceptor is Mn(IV) or Mn(III). One difficulty of modeling interfacial electron transfer from adsorbed Co(II) to structural Mn(III) is to construct realistic non-stoichiometric MnO_2 layers. Elzinga[82–84] showed that Mn(III) is labile, using ^{54}Mn radiotracers. Adsorption of Mn^{2+}_{sol} on a Mn(IV) surface site produces transient Mn(III)-Mn(III) pairs by comproportionation, which subsequently undergo disproportionation to regenerate Mn^{2+}_{sol} and Mn(IV).[82–87] Therefore, comproportionation needs to be considered in the generation of the structural models. This study is divided in two main parts. The first

part focuses on the oxidation of Co(II) in TCS position, and the second part on the oxidation of Co(II) in DCS and DES position on layer edges. Each part is divided in two sections. The first section deals with the construction of the MnO_2 layers with and without Mn(III), and the second section deals with the Gibbs free energy change (ΔG) for the complexation and oxidation of Co(II) on the surface sites of the MnO_2 models.

2. COMPUTATIONAL METHODS

Calculations were performed on cluster models with ORCA 5.0.2[88] using a computational methodology detailed previously for the complexation energies of Ni(II), Cu(II), Zn(II), and Pb(II) on birnessite.[81] Briefly, the DFT hybrid functional PBE0[89,90] together with the atom-pairwise dispersion correction D3BJ[91] has been used. The electronic configurations of all atoms were treated with the all-electron polarized def2-TZVP basis sets of triple ζ quality,[92] in combination with the Coulomb fitting auxiliary def2 /J basis sets.[93] Frequency calculations were carried out at 1 atm and 298.15 K on cluster models geometrically optimized with a convergence criterium of 10^{-8} Eh between two SCF cycles (TightSCF). The water solvent was modeled with the continuum solvent model SMD,[94] and all energies reported are free energies in solution (i.e., sometimes denoted as ΔG^*) and in kcal/mol. The proton solvation energy was taken to be −264.0 kcal/mol.[95] The potential energy surface of Co(II) involved along the TCS → INC reaction was calculated by the stepwise (n = 18) reduction of the dihedral angle of Co(II) with three layer Mn atoms. The energetics of the Co(II) → Co(III) electron transfer was modeled using the minimum energy crossing point (MECP) procedure proposed by Harvey et al.[96], as implemented with the SurfCrossOpt keyword in ORCA.

The accuracy of prediction of ΔG has been benchmarked previously[81] with the first hydrolysis constants of the hexahydrated Mn^{2+}, Ni^{2+}, and Zn^{2+} ions.[97] It was shown that ΔG values for these ions are calculated reliably within chemical accuracy (1−2 kcal/mol). For example, the experimental and calculated pK_a values for Mn^{2+} are 10.6 and 11.3, respectively. The method accuracy was further validated here with Co^{2+}: pK_a(exp) = 9.7 ± 1[98], corresponding to ΔG = 13.2 kcal/mol, and pK_a(calc.) = 11.5, corresponding to ΔG = 15.65 kcal/mol. Therefore, the computational procedure probably tends to overestimate ΔG values by approximately 2.5 kcal/mol. The total electronic charges of the cluster models, and their Mulliken atomic spin densities and multiplicities are listed in Table S1.

3. RESULTS

3.1. Co(II) oxidation on basal surfaces

3.1.1. Cluster models. The active sites on basal surfaces are Mn(IV) vacancies. Four birnessite nanolayers composed of 10 octahedral sites in the layer plane were generated (Figure 2). Nanolayers 1 and 2 will be used to test reactions 1 and 2, respectively. The first nanolayer has one Mn(III) in the layer plane (Mn^{3+}_{Layer}) and a fully protonated vacancy. It is denoted as $Mn^{3+}_{Layer}Mn^{4+}_{8}V$ and has for composition $Mn_9O_{32}H_{26}$. The second nanolayer has only Mn(IV) in the layer plance (Mn^{4+}_{Layer}) and a vacancy capped by a Mn(III) cation on one side (Mn^{3+}_{TCS}) and protonated on the other side. It is denoted as $Mn^{3+}_{TCS}Mn^{4+}_{9}V$ and has for composition $Mn_{10}O_{35}H_{30}$. The third nanolayer also has only Mn^{4+}_{Layer} in the layer plane, but no Mn^{3+}_{TCS}. It is denoted as $Mn^{4+}_{9}V$ and has for composition $Mn_9O_{32}H_{26}$. The fourth nanolayer differs from nanolayer 2 by the replacement of Mn^{3+}_{TCS} with Mn^{2+}_{TCS}, and has for composition $Mn_{10}O_{35}H_{30}$. This configuration was unstable, Mn(II) underwent comproportionation with a Mn^{4+}_{Layer} to form a $Mn^{3+}_{TCS} - Mn^{3+}_{Layer}$ pair. The total energy decreased by 1 kcal/mol when the Mn(III) cations were antiferromagnetically coupled. The antiferromagnetic model is denoted as $Mn^{3+\downarrow}_{TCS}Mn^{3+\uparrow}_{Layer}Mn^{4+}_{8}V$.

3.1.2. Energetics of the oxidation pathways. All oxidation pathways that were explored are listed in Table 1 with their ΔG value. According to the mass action law, a reaction with $\Delta G > 0$ can be favorable above a given pH when protons are released. In this case, the ratio of the concentrations of the reactant (R) and product (P) at pH 4 and 7 was calculated from $[P]/[R] = K_{eq}/[H^+]^n$, where K_{eq} is the equilibrium constant of the reaction ($\ln K_{eq} = -\Delta G/RT$).

In reaction 1,[75] Co^{2+}_{Sol} sorbs on a free vacancy bordered by five Mn^{4+}_{Layer} and one Mn^{3+}_{Layer}. Co^{2+}_{Sol} is oxidized by Mn^{3+}_{Layer}, and Co^{3+}_{TCS} migrates into the vacancy (Co^{3+}_{INC}) while Mn^{2+}_{Layer} either moves in TCS position (Mn^{2+}_{TCS}, pathway 1a) or is released in solution (Mn^{2+}_{sol}, pathway 1b) (Figure 3). Pathway 1a has ΔG = 4.4 kcal/mol and a net-zero H^+ balance, whereas pathway 1b has ΔG = 4.2 kcal/mol and consumes two H^+. Therefore, reaction 1 is thermodynamically unfavorable. As an aside, we note that the Mn^{2+}_{TCS}-Co^{3+}_{INC} pair formed in pathway 1a was stable; Mn^{2+}_{TCS} did not comproportionate with a Mn^{4+}_{Layer} in this configuration.

In reaction 2a,[75] Co^{2+}_{Sol} is oxidized to Co^{3+}_{TCS} by Mn^{3+}_{TCS}, which is reduced to Mn^{2+}_{Sol} (Figure 4). Afterward, Co^{3+}_{TCS} migrates into the vacancy (Co^{3+}_{INC}) releasing the two H^+ located on the other side of the vacancy (pathway 2b). Pathway 2a has a highly positive ΔG value of 17.1 kcal/mol, and pathway 2b has ΔG = -17.7 kcal/mol and $[Co^{3+}_{INC}]/[Co^{3+}_{TCS}] = 9.4 \times 10^{26}$ at pH 7. Pathway 2a is thermodynamically prohibited, wheareas pathway 2b is spontaneous. If a Co(III) occurs on a vacancy, it will immediately fill it. Reaction 3[26] occurs on lateral surfaces and will be examined in the following section.

In reaction 4, Co^{2+}_{Sol} sorbs on a free vacancy and Co^{2+}_{TCS} is oxidized to Co^{3+}_{INC} by a Mn^{4+}_{Layer}, which is reduced to Mn^{3+}_{Layer}. The net proton balance of the oxidation reaction is -2 if the two H^+ located on the other side of the vacancy are released in solution (pathway 4a), or zero if the H^+ release is balanced by the adsorption of two H^+ on the undersaturated oxygens shared by the $[Co^{3+}O_6]$ and $[Mn^{3+}O_6]$ octahedra (pathway 4b, Figure 5). Pathway 4a has ΔG = 16.9 kcal/mol and $[Co^{3+}_{INC}]/[Co^{2+}_{TCS}]$ = 40.9 at pH 7, and pathway 4b has ΔG = -5.2 kcal/mol and $[Co^{3+}_{INC}]/[Co^{2+}_{TCS}] = 6.5 \times 10^3$, regardless of pH. Correcting the two ΔG values by the estimated 2.5 kcal/mol overestimation of the calculation (section 2) yields ΔG = 14.4 kcal/mol and $[Co^{3+}_{INC}]/[Co^{2+}_{TCS}] = 2.8 \times 10^3$ at pH 7 for pathway 4a, and ΔG = -7.7 kcal/mol and $[Co^{3+}_{INC}]/[Co^{2+}_{TCS}] = 3.1 \times 10^5$ for pathway 4b. This Co(II) oxidation pathway is thermodynamically favorable.

In reaction 5, Co^{2+}_{Sol} replaces $Mn^{3+\downarrow}_{TCS}$ in the antiferromagnetic $Mn^{3+\downarrow}_{TCS}Mn^{3+\uparrow}_{Layer}$ pair, forming a Co^{2+}_{TCS} complex, while $Mn^{3+\downarrow}_{TCS}$ is reduced to Mn^{2+}_{Sol} by $Mn^{3+\uparrow}_{Layer}$, which is oxidized to Mn^{4+}_{Layer} (Figure 5). Afterward, Co^{2+}_{TCS} is oxidized following the reaction 4 pathway. In this mechanism, adsorption of Co^{2+}_{sol} reverses the $Mn^{2+}_{TCS}Mn^{4+}_{Layer} \rightarrow Mn^{3+\downarrow}_{TCS}Mn^{3+\uparrow}_{Layer}$ comproportionation reaction, and Co^{2+}_{Sol} substitutes for Mn^{2+}_{TCS} according to the $Co^{2+}_{Sol}Mn^{2+}_{TCS} \leftrightarrow Co^{2+}_{TCS}Mn^{2+}_{Sol}$ exchange reaction. Reaction 5 is thermodynamically favorable with ΔG = -6.7 kcal/mol. We verified that Co^{2+}_{Sol} is not oxidized by $Mn^{3+\downarrow}_{TCS}$ in this configuration, as is the case for pathway 2a when Mn^{3+}_{TCS} is not paired with a Mn^{3+}_{Layer}. Here, ΔG of $Mn^{3+\downarrow}_{TCS}Mn^{3+\uparrow}_{Layer} \rightarrow Co^{3+}_{TCS}Mn^{3+}_{Layer}$ is 22.0 kcal/mol compared to 17.1 kcal/mol for pathway

2a. Oxidation of Co(II) on Mn(III)-capped vacancies will be slower than on vacancy sites freed from interlayer Mn(III).

Because the nanolayers are treated as molecules in DFT geometry-optimization, small cluster models with a vacancy can experience too much relaxation that would not occur to mineral (nano)particles, and therefore would lead to wrong interpretation. This cautionary tale was addressed by increasing to 23 [MnO_6] octahedra the size of the nanolayer and by calculating the ΔG values of reaction 5 ($Mn^{3+\downarrow}_{TCS}Mn^{3+\uparrow}_{Layer}Mn^{4+}_{22}V \rightarrow Co^{2+}_{TCS}Mn^{4+}_{23}V$) (Figure S1). ΔG(5) = -6.3 kcal/mol for the $Mn_{23}V$ model compared to ΔG(5) = -6.7 kcal/mol for the Mn_9V model (Table 1).

3.1.3. Oxidation mechanism of Co(II) on vacancies. To be examined now is how Co(II) enters the vacancy site and is oxidized by Mn(IV) during reaction 4 ($Co^{2+}_{TCS}Mn^{4+}_{Layer} \rightarrow Co^{3+}_{INC}Mn^{3+}_{Layer}$). We interrogated first if the electron transfer occurred between Co^{2+}_{TCS} and Mn^{4+}_{Layer} before the entry into the vacancy site. This was performed by optimizing the geometry of $Co^{3+}_{TCS}Mn^{3+}_{Layer}Mn^{4+}_{8}V$, with the d^6 Co^{3+} ion in low-spin state ($t_{2g}{}^6e_g{}^0$, S = 1), and the d^4 Mn^{3+} and d^3 Mn^{4+} ions in high-spin state ($t_{2g}{}^3e_g{}^1$, S = 5; $t_{2g}{}^3e_g{}^0$, S = 4, respectively, S_{tot} = 29). On analysis of the spin electronic densities (ρ) obtained through the Mulliken population analysis, Co had ρ = 0.94 (S ~ 2) and all the Mn atoms had ρ ~ 3 (S ~ 4) in the optimized structure. Thus, the thermodynamically most stable complex is $Co^{2+,LS}_{TCS}Mn^{4+}_{9}V$ when the total spin is 29, with the d^7 Co^{2+} ion in low-spin state ($t_{2g}{}^6e_g{}^1$, S = 2), instead of its usual high-spin state ($t_{2g}{}^5e_g{}^2$, S = 4). The unpaired electron in the e_g orbitals of low-spin Co(II) leads to a Jahn-Teller distortion of the $[Co^{2+}_{TCS}O_3(H_2O)_3]$ octahedron with d(Co-O_{2Mn}) = 1.96 Å, 1.99 Å, 2.14 Å and d(Co-H_2O) = 2.04 Å , 2.05 Å , 2.22 Å. Still, a stable $Co^{3+}_{TCS}Mn^{3+}_{Layer}Mn^{4+}_{8}V$ complex could be obtained by enforcing a Mn(III) octahedron in the layer, but the total electronic energy of the complex was 12 kcal/mol higher than that of $Co^{2+,LS}_{TCS}Mn^{4+}_{9}V$.

This finding suggests that the $Co^{2+,LS}_{TCS}Mn^{4+}_{9}V$ complex may be a stable intermediate state, in which Co(II) now possesses a single unpaired electron, which is transferred to Mn^{4+}_{Layer} yielding the $Co^{3+}_{INC}Mn^{3+}_{Layer}Mn^{4+}_{8}V$ reaction product. The $Co^{2+,LS}_{TCS}Mn^{4+}_{9}V$ complex is ΔG = 19.2 kcal/mol higher in energy than the $Co^{2+}_{TCS}Mn^{4+}_{9}V$ reactant complex. The $Co^{3+}_{TCS}Mn^{3+}_{Layer}Mn^{4+}_{8}V$ complex is further higher with

ΔG = 28.7 kcal/mol. We show below with a PES scan, that the hypothesis of a $Co^{2+}_{TCS}Mn^{4+}_{Layer} \rightarrow Co^{2+,LS}_{TCS}Mn^{4+}_{Layer} \rightarrow Co^{3+}_{INC}Mn^{3+}_{Layer}$ reaction pathway is not supported.

The reactant complex (R) of the PES scan was $Co^{2+}_{TCS}Mn^{4+}_{9}V_d$ (S_{tot} = 31) and the product complex (P) was $Co^{2+}_{INC}Mn^{4+}_{9}$ with the two protons from the opposite side of the vacancy removed to avoid obstructing the migration of Co (V_d denotes a deprotonated vacancy). Note that the spin state cannot be changed during a PES scan. The PES has a double-hump profile, characteristic of the occurrence of an intermediate product (IP1) bracketed by two transition states (TS1, TS2) (Figure 6). The IP1 state is a tetrahedral complex ($^{IV}Co^{2+}_{TCS}Mn^{4+}_{9}V_d$), in which Co(II) is bonded to the three surface O_{2M} atoms at 1.92-1.95 Å and one water molecule at 2.06 Å, and resides in the high-spin state (Figure 7). The transition from the octahedral to the tetrahedral coordination occurs via the loss of a first water molecule on the way to TS1. In the actual transition state (Video S1), a second coordination bond between a water molecule and Co^{2+} is broken (ν = 98 *i* cm^{-1}, single negative frequency calculated at PBE0/tzvp-D3BJ level), providing a tetrahedral complex (IP1) behind. In IP1, the two expelled water molecules are hydrogen bonded to the oxygen atom of the remaining water molecule coordinated to Co^{2+}. The penetration of $^{IV}Co^{2+}_{TCS}$ in the vacancy is shown in Video S2, which represents the imaginary frequency of TS2 (ν = 1308 *i* cm^{-1}, single negative frequency calculated at PBE0/tzvp-D3BJ level). The three surface O_{2M} atoms move away from Co (d(Co-O_{2M}) = 2.01-2.10 Å) to enlarge the effective size of the trigonal aperture, while the three basal O_{2M} atoms move upward to d(Co-O_{2M}) = 2.3-2.5 Å to bond the entering Co atom. ^{IV}Co(II) looses its water molecule when the distance to the basal O_{2Mn} atoms is 2.2 Å. At this step, Co(II) is located slightly below the surface oxygen plane of the octahedral cavity with d(Co-O_{2Mn}) = 2.0 Å. Animations of the PES scans for the $Co^{2+}_{TCS}Mn^{4+}_{9}V_d \rightarrow Co^{2+}_{INC}Mn^{4+}_{9}$ and the $Co^{2+}_{TCS}Mn^{4+}_{23}V_d \rightarrow Co^{2+}_{INC}Mn^{4+}_{23}$ pathways can be viewed in Videos S3, and S4, respectively.

The first potential energy barrier is $\Delta E(\text{TS1-R})^{\ddagger}$ = 7.2 kcal/mol relative to R, and the second is $\Delta E(\text{TS2-IP1})^{\ddagger}$ = 3.0 kcal/mol relative to IP1 (Figure 6). The Gibbs free energy differences $\Delta G^{\ddagger}$(TS1-R), $\Delta G^{\ddagger}$(TS2-IP1), and ΔG(IP1-R) were calculated to be 4.4 kcal/mol, 2.4 kcal/mol, and -0.4 kcal/mol, respectively (reaction 7a, Table 1, Figures 7 and S2).

The release of the two basal protons located on the other side of the Mn(IV) vacancy during the migration of Co(II) is challenging to model, and therefore was omitted. A sense of how much they modify the energetic of the $Co^{2+}_{TCS} \rightarrow {}^{IV}Co^{2+}_{TCS}$ reaction was obtained by calculating the PES scan with

two protons bonded to the basal O_{2Mn} atoms. The energy difference between IP1 and R increased from -0.4 kcal/mol to 4.2 kcal (reaction 7b, Table 1, and Figure S2), and d(Co-O_{2Mn}) increased from 1.92-1.95 Å to 1.94-1.96 Å. In real situation where the vacancy is protonated, the two basal protons are likely released during the migration of the tetrahedral complex into the octahedral cavity, and they raise the TS1 barrier from $\Delta E^{\ddagger}$(TS1-R) = 7.2 kcal/mol to $\Delta E^{\ddagger}$(TS1-R) = 19.4 kcal/mol, but not the TS2 barrier relative to IP1 ($\Delta E^{\ddagger}$(TS2-IP1) = 3.0 kcal/mol).

Modeling of the oxidation state switching of Co(II) and Mn(IV) after the MECP procedure of Harvey et al.[96] shows that Co(II) undergoes a spin flip inside the vacancy allowing for interconversion between the quartet (S = 4) $t_{2g}^5e_g^2$ spin state and the doublet (S = 2) $t_{2g}^6e_g^1$ spin state (Figure 7). The Gibbs free energy of the $Co^{2+}_{TCS}Mn^{4+}_{Layer} \rightarrow Co^{2+,LS}_{INC}Mn^{4+}_{Layer}$ reaction is ΔG = 0.1 kcal/mol when protons are omitted (reaction 8, Table 1, and Figure S2). Finally, Co^{3+}_{INC} is formed through the energetically favorable reaction $Co^{2+,LS}_{INC}Mn^{4+}_{INC} \rightarrow Co^{3+,LS}_{INC}Mn^{3+}_{INC}$ (ΔG = -17.7 kcal/mol, Figure 7).

3.2. Co(II) oxidation on lateral surfaces

3.2.1. Cluster models. Two birnessite nanolayers composed of 7 octahedral sites were generated (Figure 8). Nanolayer 1 has one Mn^{3+}_{Layer} at the surface and will be used to test reaction 3, and nanolayer 2 has only Mn^{4+}_{Layer} and will be used to test the oxidation of Co(II) by a surface Mn(IV). Nanolayer 1 is denoted as $Mn^{3+}_{Layer}Mn^{4+}_{6}$, nanolayer 2 is denoted as Mn^{4+}_{7}, and they both have for composition $Mn_7O_{24}H_{18}$. The [MnO_6] octahedra exposed to the surface share two (DES linkage) or three (TES linkage) edges with the nearest octahedra, and therefore a surface Mn(III) cation may occupy two positions in nanolayer 1. This cation results most likely from the comproportionation of a sorbed Mn(II) cation on the DES or TES surface sites and a layer Mn(IV) cation. Therefore, the linkage of Mn^{3+}_{Layer} in nanolayer 1 was assessed by optimizing the structure of a $Mn^{2+}_{DES}Mn^{4+}_{7}$ and a $Mn^{2+}_{TES}Mn^{4+}_{6}$ nanolayer (Figure S3) A Mn^{2+}_{DES} complex is stable, whereas a Mn^{2+}_{TES} complex undergoes comproportionation with a Mn^{4+}_{Layer} to form a $Mn^{3+}_{TES}Mn^{3+}_{Layer}$ pair. Therefore, the surface Mn(III) cation was placed in TES position in nanolayer 1 (Figure 8a).

3.2.2. Energetics of surface complexation and oxidation pathways. Co(II) can form a DCS or a DES complex on nanolayers 1 and 2 (Figure 9). The two complexes are bonded to one Mn^{3+}_{Layer} and to one Mn^{4+}_{Layer} in nanolayer 1 ($Mn^{3+}_{Layer}Mn^{4+}_{6}$), and to two Mn^{4+}_{Layer} in nanolayer 2 (Mn^{4+}_{7}) (Figures 9 and S4). The Gibbs free energies of complexation of the four configurations are: $\Delta G(Co^{2+}_{DCS}\text{-}Mn^{3+}_{Layer}Mn^{4+}_{6})$ = -23.2 kcal/mol; $\Delta G(Co^{2+}_{DCS}\text{-}Mn^{4+}_{7})$ = -16.5 kcal/mol; $\Delta G(Co^{2+}_{DES}\text{-}Mn^{3+}_{Layer}Mn^{4+}_{6})$ = -12.1 kcal/mol; $\Delta G(Co^{2+}_{DES}\text{-}Mn^{4+}_{7})$ = -18.1 kcal/mol (Figure S4). Co(II) has a higher affinity for Mn(III) than for Mn(IV) in DCS position, and a higher affinity for Mn(IV) than for Mn(III) in DES position. Complexation on a DES site releases one proton, and no proton on a DCS site. At pH 7, the calculated $[Co^{2+}_{DCS}\text{-}Mn^{3+}_{Layer}Mn^{4+}_{6}]/[Mn^{2+}_{Sol}]$ ratio is 1.0×10^{17}, and the $[Co^{2+}_{DES}\text{-}Mn^{4+}_{7}]/Mn^{2+}_{Sol}]$ ratio is 1.8×10^{20}. Therefore, formation of a DES complex is preferred over that of a DCS complex, as is the case for the complexation of Ni(II), Cu(II), and Zn(II).[81]

In the oxidation reaction 3, solvated Co(II) forms a Co^{2+}_{DCS} complex on a $Mn^{3+}_{Layer}Mn^{4+}_{6}$ surface site, transfers an electron to Mn^{3+}_{Layer}, which is reduced to Mn^{2+}_{Sol}, and the oxidized Co^{3+}_{DCS} species fills the vacant Mn^{3+}_{Layer} site (Figure 9a).[26] This pathway is thermodynamically unfavorable with ΔG = 34.1 kcal/mol (Table 1). Mn^{4+}_{Layer} is the oxidant in reactions 9 and 10, and the reduced Mn^{3+}_{Layer} cation remains in the structure forming a Co^{3+}_{Layer} - Mn^{3+}_{Layer} pair (Figures 9b,c). Reaction 9 involves a Co^{2+}_{DCS} complex and has ΔG = 19.5 kcal/mol and reaction 10 involves a Co^{2+}_{DES} complex and has ΔG = 21.1 kcal/mol. The two pathways are also thermodynamically unfavorable. Other pathways were tested, but we could not find any which was energetically favorable on lateral surfaces.

4. DISCUSSION

Computational chemistry reveals an evolving new view of the oxidation mechanism of Co(II) on hexagonal birnessite. According to the predictive thermodynamic models explored in this study, Co(II) is not oxidized on MnO_2 layer edges but on vacancy sites on basal planes. Vacancy sites are known to form strong TCS complexes with divalent metals, and to be involved in electron exchange reaction with Mn(III) and Mn(IV).[11,19,20,33,43,54–60,69,70,78,99–123] They facilitate photoconductivity and photoreductive dissolution of the MnO_2 layer.[82,99,124] Although Mn(III) has a strong electron affinity

and is usually regarded to mediate the oxidative activity of birnessite, whether it is bonded over a vacancy (Mn^{3+}_{TCS}) or is incorporated in the lattice (Mn^{3+}_{Layer}),[82–84,125–131] our results are at odds with that interpretation for the oxidation of Co(II) to Co(III). We found that Co(II) sorbed on a vacancy site (Co^{2+}_{TCS}) is oxidized to Co^{3+}_{INC} by a layer Mn(IV) in the vacancy. This molecular mechanism is consistent with the increase in Mn(III) content measured by XPS.[39,28]

Co(II) undergoes successively a coordination change from octahedral ($^{VI}Co^{2+}_{TCS}Mn^{4+}_{Layer}$) to tetrahedral ($^{IV}Co^{2+}_{TCS}Mn^{4+}_{Layer}$) to enter the vacancy site followed by a quartet ($t_{2g}^5e_g^2$, S = 4) to doublet ($t_{2g}^6e_g^1$, S = 2) to singlet ($t_{2g}^6e_g^0$, S = 1) spin transition during its oxidation to Co(III). The potential energy barriers for the octahedral to tetrahedral conversion ($Co^{2+}_{TCS}Mn^{4+}_{Layer} \rightarrow {}^{IV}Co^{2+}_{TCS}Mn^{4+}_{Layer}$, TS1) and for the penetration of the tetrahedral complex into the vacancy (TS2) are as low as $\Delta E^{\ddagger}$ = 7.2 kcal/mol and 3.0 kcal/mol, respectively. This can be understood in light of the d^7 electronic configuration of Co(II) with regard to that of Ni(II) (d^8), which can also enter the vacancy sites.[54,57,132] The TS1 and TS2 barriers of Ni are 14.4 kcal/mol and 3.0 kcal/mol, respectively (Figure 6). The 7.2 kcal/mol difference in height of the TS1 state for Co and Ni can be explained with reference to their difference of crystal field stabilization energy (CFSE) in octahedral and tetrahedral coordination. An electron gains -0.4 Δ in one of the orbitals of the t_{2g} levels and looses +0.6 Δ in one of the orbitals of the e_g levels, where Δ is the crystal field splitting parameter.[133] A high-spin Co^{2+} ion acquires a CFSE of -0.8 Δ_{oct} in octahedral coordination and -1.2 Δ_{tet} in tetrahedral configuration, and a high-spin Ni^{2+} ion acquires, respectively, a CFSE of 1.2 Δ_{oct} and -0.8 Δ_{tet}. Taking $\Delta_{tet} = 4/9\ \Delta_o$,[133] we can calculate the difference in CFSE between octahedral and tetrahedral geometries by referencing everything in terms of Δ_{oct}. The net difference is 0.27 Δ_{oct} for Co(II) and 0.85 Δ_{oct} for Ni(II), and therefore the gap between the two coordinations and height of the TS1 state are smaller for Co(II) than for Ni(II).

Turning to the height of the TS2 state, the close correspondance for Co(II) and Ni(II) can be explained now with reference to the similarity of their effective ionic radii in tetrahedral coordination with $r(^{IV}Co^{2+}$ = 0.58 Å) and $r(^{IV}Ni^{2+}$ = 0.55 Å).[134] The decrease in size of Co(II) and Ni(II) resulting from the octahedral to tetrahedral coordination change facilitates the passage through the small triangular-shaped aperture delimited by the three O_{2Mn} atoms at the surface of the MnO_2 layer.

The d^7 electronic structure of Co(II) also confers special characteristics on Co(II) systems regarding the interconversion between the high-spin ($t_{2g}^5e_g^2$, S = 4) and the low-spin ($t_{2g}^6e_g^1$, S = 2) states. Unpaired electrons can easily undergo spin inversion and both spin states configurations are known in

six-coordinate Co(II) complexes.[135] The single electron in the e_g orbitals induces a strong Jahn-Teller effect inside the vacancy site with predicted d(Co-O_{eq}) = 1.88-1.90 Å and d(Co-O_{ax}) = 2.27 Å. A significant result is that the intermediate $Co^{2+,LS}_{INC}Mn^{4+}_{9}V$ complex is thermodynamically as stable as the initial $Co^{2+}_{TCS}Mn^{4+}_{9}V$ complex (ΔG = 0.1 kcal/mol). Formation of the $Co^{2+,LS}_{INC}Mn^{4+}_{9}V$ complex is followed by an electron transfer from a low-spin Co^{2+} ion to a high-spin Mn^{4+} ion ($t_{2g}^3e_g^0$), which is reduced to high-spin Mn^{3+} ($t_{2g}^3e_g^1$) while Co^{2+} is oxidized to low-spin Co^{3+} ($t_{2g}^6e_g^0$). The Co^{3+}-O distances of the resulting [CoO_6] octahedron are regular (d(Co-O) = 1.90-193 Å), whereas the Mn^{3+}-O distances are distinctive of a Jahn-Teller distorsion with d(Mn-O_{eq}) = 1.90-1.92 Å and d(Mn-O_{ax}) = 2.19-2.21 Å. The close match between the low-spin Co^{2+}-O and high-spin Mn^{3+}-O distances is consistent with the similarity of the ionic radii for the two metal ions (low-spin Co^{2+} = 0.65 Å, high-spin Mn^{3+} = 0.645 Å).[134] Formation of the low-spin $t_{2g}^6e_g^1$ Co(II) configuration makes it easier for an e_g electron to transfer to the e_g orbitals of a $t_{2g}^3e_g^0$ Mn^{4+} ion and stabilization of the final $t_{2g}^6e_g^0$ Co(III) - $t_{2g}^3e_g^1$ Mn(III) configuration. The oxidation state switching is predicted to be highly exergonic (ΔG = -17.6 kcal/mol). The question remains as to which reaction step is rate limiting in the stepwise $Co^{2+}_{TCS}Mn^{4+}_{Layer} \xrightarrow{TS1} {}^{IV}Co^{2+}_{TCS}Mn^{4+}_{Layer} \xrightarrow{TS2} Co^{2+,LS}_{INC}Mn^{4+}_{Layer} \rightarrow Co^{3+}_{INC}Mn^{3+}_{Layer}$ redox reaction.

The release in solution of Mn(II) that accompanies the oxidation of Co(II) is interpreted usually as evidence for Mn(III) acting as the electron acceptor. In the new model, aqueous Mn(II) measured by chemical analysis during the oxidation of Co(II) results, at least partly, from the stepwise disproportionation of $Mn^{3+}_{TCS}Mn^{3+}_{Layer}$ into $Mn^{2+}_{TCS}Mn^{4+}_{Layer}$ followed by the substitution of Co^{2+}_{TCS} for Mn^{2+}_{TCS} and release of Mn(II) to solution. The chemical formula of well-crystallized hexagonal birnessite is typically $H^{+}_{0.33}Mn^{3+}_{0.111}Mn^{2+}_{0.055}(Mn^{4+}_{0.722}Mn^{3+}_{0.11}\square_{0.167})O_2 \cdot (H_2O)_{0.50}$ at pH 5,[74] and the chemical formula of Na-exchanged δ-MnO_2 is typically $H^{+}_{0.16}Na^{+}_{0.18}Mn^{3+}_{0.15}(Mn^{4+}_{0.72}Mn^{3+}_{0.11}\square_{0.17})O_2 \cdot (H_2O)_{0.75}$ at pH 6.[80] The [Mn^{3+}_{TCS}]/[Mn^{3+}_{Layer}] ratio is close to one, which suggests that the majority of the Mn(III) cations are formed by comproportionation of a Mn^{2+}_{TCS} and Mn^{4+}_{Layer}, yielding discrete Mn^{3+}_{TCS}-Mn^{3+}_{Layer} pairs in the structure. These pairs are metastable,[83] and the comproportionation reaction is reverted in the presence of Co(II) (ΔG = -6.7 kcal/mol, reaction 5, Table 1). DFT calculations show that Mn^{2+}_{TCS} is also replaced with Ni(II) (ΔG = -6.3 kcal/mol), Cu(II) (ΔG = -6.9 kcal/mol), and Zn(II) (ΔG = -7.5 kcal/mol). These metals inhibit formation of Mn(III) through comproportionation.[136,137]

Aqueous Mn(II) may also result from the disproportionation of two Mn^{3+}_{Layer}. According to the proposed oxidation mechanism, Mn^{3+}_{Layer} build up with time in the MnO_2 layer, and therefore could be subject to $Mn^{3+}_{Layer}Mn^{3+}_{Layer} \rightarrow Mn^{4+}_{Layer} + \square + Mn^{2+}_{sol}$ disproportionation, as occurs in the conversion of buserite (10 Å birnessite) to hexagonal birnessite.[43] This mechanism may explain the decrease of the amount of Jahn-Teller distorted Mn(III) octahedra in Co(II)-reacted birnessite at high Co/(Co+Mn) molar ratios.[30] Should this be the case, the disproportionation reaction would create Mn^{4+}_{Layer}-vacancy pairs capable of oxidizing new Co^{2+} ions. The reaction can be written

$$Co^{2+}_{Sol} + \square_1 + Mn^{3+}_{Layer}Mn^{4+}_{Layer} \rightarrow Co^{3+}_{INC}Mn^{3+}_{Layer}Mn^{3+}_{Layer} \rightarrow Co^{3+}_{INC}Mn^{4+}_{Layer} + \square_2 + Mn^{2+}_{Sol}$$

and is equivalent to the balanced reaction 1. A similar mechanism with production of new vacancy sites was proposed for the oxidation of Cr(III) to Cr(VI) by birnessite.[103]

Existence of an intermediate low-spin Co(II) species in the oxidation pathway on vacancy sites provides a hint for the lack of oxidation on the edge sites. Co(II) switches easily between the high- and low-spin states in inorganic complexes depending on the molecular environment.[135,138] In the case of birnessite, the $t_{2g}^5e_g^2 \rightarrow t_{2g}^6e_g^1$ spin transition is likely driven by the dimension of the empty Mn(IV) layer site. This site can accommodate a Mn^{3+} ion having a size of 0.645 Å compared to 0.53 Å for Mn^{4+}.[42] With a size of 0.65 Å, a low-spin Co^{2+} ion is a better match to the dimension of the vacancy than a high-spin Co^{2+} ion (r = 0.745 Å).[134] The $t_{2g}^6e_g^1$ electronic configuration of low-spin Co(II) enforced by steric constraints facilitates the electron transfer to the unoccupied e_g orbitals of Mn(IV). Steric constraints do not exist on edge sites, and high-spin Co(II) is the stable conformation (reaction 10, Figure 9c, Table 1). Therefore, the $t_{2g}^6e_g^1$ electronic configuration of low-spin Co(II) appears to be key condition for the transfer of an electron between the e_g orbitals of Co(II) and Mn(IV), a condition which is not fulfilled on the edge sites.

Results of this study call into question the proposal by Simanova and Peña[26] that oxidation occurs on both the MnO_2 edges and layer vacancies. The number of Mn atoms measured by EXAFS spectroscopy in the nearest (CN(ES)) and next-nearest (CN(CS)) shells increased from CN(ES) = 3.12 ± 0.49 and CN(CS) = 2.71 ± 0.43 after 7 min reaction time to CN(ES) = 4.13 ± 0.62 and CN(CS) = 5.39 ± 1.76 after 12 h reaction time at low surface coverage (Co/Mn = 0.05). Because EXAFS coordination numbers are averaged over all Co atoms present and are normalized on a per Co basis, CN(ES) = 3.12 ± 0.49 and CN(CS) = 2.71 ± 0.43 can be interpreted as about 50% Co atoms in TCS position (CN(CS) = 6) and 50% in INC position (CN(ES) = 6) within uncertainty. CN values obtained

after 12 h reaction time are problematic. The sum of Mn neighbors (4.13 + 5.39 = 9.52) exceeded the structural maximum of 6, even after consideration of uncertainty ((4.13-0.62) + (5.39-1.76) = 7.14). In addition, the majority of the Debye-Waller parameters (σ), which account for the distribution of interatomic distances, were lower for the Co-Mn shells than for the Co-O shells. This is physically unrealistic because structural order decreases (i.e., σ increases) with radial distance in solid matter. Furthermore, the Co-CS distance decreased from 3.48-3.50 Å after 66 min reaction time to 3.43 Å after 12 h. The shortening was attributed to Co^{3+}_{TCS}-$Mn^{3+/4+}_{Layer}$ atomic pairs resulting from the oxidation of Co(II) by interlayer Mn(III) with formation of a Co(III)-TCS complex and release of Mn^{2+}_{Sol} (reaction 2a). This pathway is thermodynamically unfavorable (ΔG = 17.1 kcal/mol). The Co-Mn distance of 3.43 Å can be attributed instead to Co^{3+}_{INC}-Mn^{3+}_{TCS} atomic pairs formed at longer reaction times by the readsorption and comproportionation of Mn^{2+}_{Sol} on vacancy sites adjacent to Co^{3+}_{INC}. Therefore, in our opinion the DFT results do not necessarily conflict with the EXAFS data of Simanova and Peña.[26]

In summary, extensive quantum mechanical calculations of the oxidative scavenging of Co(II) by birnessite nanolayers led us to identify two new intermediate products. One IP is a tetrahedral Co^{2+}_{TCS} complex, which facilitates the crossing of the surface oxygen layer to reach the underlying Mn(IV) cavity in reducing the effective ionic radius of Co(II). The same coordination change occurs for Ni(II). The other IP is a low-spin Co^{2+}_{INC} complex, which facilitates the electron transfer between the e_g orbitals of Co(II) and Mn(IV), producing Co(III) and Mn(III). This study also provides new insight into the origin of Mn(II) measured in solution during the oxidation reaction. DFT calculations show that the Mn^{2+}_{TCS} complex is unstable and undergoes comproportionation with a layer Mn(IV) cation, forming $Mn^{3+}_{TCS} - Mn^{3+}_{Layer}$ pairs. In the presence of Co(II), the opposite disproportionation reaction occurs, releasing Mn(II) in solution and reforming a layer Mn(IV), which subsequently may oxidize the Co^{2+}_{TCS} complex. The layer Mn(III) cations resulting from the oxidation of Co(II) may also disproportionate, producing Mn(IV) and soluble Mn(II) and creating a new vacancy site. This site may be prone to Co(II) sorption, thereby maintaining the oxidative activity of the MnO_2 layer. Results of this study will help understanding the oxidation of Co(II) to Co(III) in MnO_2-based batteries and catalysts.[139–148] Experimental studies are needed to test the effect of oxygen vacancies[149,150] on Co(II) oxidation and to allow consider this effect in DFT modeling.

ASSOCIATED CONTENT

Supporting Information

The Supporting Information is available free of charge on the ACS Publications website at DOI:

Schematic pathways and Gibbs free-energies of reactions 5, 6, 7, and 8, and of complexation of Co(II) as DCS and DES complex, geometry optimized ferromagnetic and antiferromagnetic Mn(II)-DES complex and ferromagnetic Mn(II)-TES complex, and Cartesian coordinates of the $Mn^{3+\downarrow}_{TCS}Mn^{3+\uparrow}_{Layer}Mn^{4+}_{8}V$, $Co^{2+}_{TCS}Mn^{4+}_{9}V$, $Co^{3+}_{INC}Mn^{3+}Mn^{4+}_{8}$, $^{IV}Co^{2+}_{TCS}Mn^{4+}_{9}V$, $^{IV}Co^{2+}_{TCS}Mn^{4+}_{9}V_{d}$, and $Co^{2+,LS}_{INC}Mn^{4+}_{9}$ complexes (PDF)

Potential energy surfaces and transition states TS1 and TS2 (AVI, AVI, AVI, AVI)

AUTHOR INFORMATION

Corresponding Author

E-mail: alain.manceau@univ-grenoble-alpes.fr

ORCID

Alain Manceau: 0000-0003-0845-611X

Stephan N. Steinmann: 0000-0002-2777-356X

Notes

The authors declare no competing financial interests.

ACKNOWLEDGEMENTS

The GRICAD laboratory from the University Grenoble Alpes provided computing resources, and Pierre Girard gave his expertise in parallel scientific processing. Three anonymous reviewers are acknowledged for constructive comments on the manuscript.

REFERENCES

(1) Taylor, R. M.; McKenzie, R. M. The Association of Trace Elements with Manganese Minerals in Australian Soils. *Aust. J. Soil. Res.* **1966**, *4*, 29–39.

(2) Burns, R. G.; Burns, V. M. Mineralogy of Ferromanganese Nodules. In *Marine Manganese Deposits*; Glasby, G. P., Ed.; 1977; pp 185–248.

(3) Lienemann, C. P.; Taillefert, M.; Perret, D.; Gaillard, J. F. Association of Cobalt and Manganese in Aquatic Systems: Chemical and Microscopic Evidence. *Geochim. Cosmochim. Acta* **1997**, *61*, 1437–1446.

(4) Koschinsky, A.; Hein, J. R. Uptake of Elements from Seawater by Ferromanganese Crusts: Solid-Phase Associations and Seawater Speciation. *Mar. Geol.* **2003**, *198*, 331-351.

(5) Hein, J. R.; Mizell, K.; Koschinsky, A.; Conrad, T. A. Deep-Ocean Mineral Deposits as a Source of Critical Metals for High- and Green-Technology Applications: Comparison with Land-Based Resources. *Ore Geol. Rev.* **2013**, *51*, 1–14.

(6) Wegorzewski, A. V.; Kuhn, T.; Dohrmann, R.; Wirth, R.; Grangeon, S. Mineralogical Characterization of Individual Growth Structures of Mn-Nodules with Different Ni+Cu Content from Central Pacific Ocean. *Am. Miner.* **2015**, *110*, 2497–2508.

(7) Hein, J. R.; Conrad, T.; Mizell, K.; Banakar, V. K.; Frey, F. A.; Sager, W. W. Controls on Ferromanganese Crust Composition and Reconnaissance Resource Potential, Ninetyeast Ridge, Indian Ocean. *Deep Sea Res. Part I Oceanogr. Res. Pap.* **2016**, *110*, 1–19.

(8) Dublet, G.; Juillot, F.; Brest, J.; Noel, V.; Fritsch, E.; Proux, O.; Olivi, L.; Ploquin, F.; Morin, G. Vertical Changes of the Co and Mn Speciation along a Lateritic Regolith Developed on Peridotites (New Caledonia). *Geochim. Cosmochim. Acta* **2017**, *217*, 1–15.

(9) Marino, E.; Gonzalez, F. J.; Kuhn, T.; Madureira, P.; Wegorzewski, A. V.; Mirao, J.; Medialdea, T.; Oeser, M.; Miguel, C.; Reyes, J.; Somoza, L.; Lunar, R. Hydrogenetic, Diagenetic and Hydrothermal Processes Forming Ferromanganese Crusts in the Canary Island Seamounts and Their Influence in the Metal Recovery Rate with Hydrometallurgical Methods. *Minerals* **2019**, *9*, n° 439.

(10) Heller, C.; Kuhn, T.; Versteegh, G. J. M.; Wegorzewki, A. V.; Kasten, S. The Geochemical Behavior of Metals during Early Diagenetic Alteration of Buried Manganese Nodules. *Deep-Sea Res. Part I. Oceanogr. Res. Pap.* **2018**, *142*, 16–33.

(11) Wegorzewski, A. V.; Grangeon, S.; Webb, S. M.; Heller, C.; Kuhn, T. Mineralogical Transformations in Polymetallic Nodules and the Change of Ni, Cu and Co Crystal-Chemistry upon Burial in Sediments. *Geochim. Cosmochim. Acta* **2020**, *282*, 19–37.

(12) Mizell, K.; Hein, J. R.; Koschinsky, A.; Hayes, S. M. Effects of Phosphatization on the Mineral Associations and Speciation of Pb in Ferromanganese Crusts. *ACS Earth Space Chem.* **2020**, *4*, 1515–1536.

(13) Hein, J. R.; Koschinsky, A.; Kuhn, T. Deep- Ocean Polymetallic Nodules as a Resource for Critical Materials. *Nat. Rev. Earth Environ.* **2020**, *1*, 159–169.

(14) Sousa, L. M. C.; Santos, R. V.; Koschinsky, A.; Bau, M.; Wegorzewki, A. V.; Cavalcanti, J. A. D.; Dantas, E. L. Mineralogy and Chemical Composition of Ferromanganese Crusts from the Cruzeiro Do Sul Lineament - Rio Grande Rise, South Atlantic. *J. South Am. Earth Sci.* **2021**, n° 103207.

(15) Vereshchagin, O.; Perova, E.; Brusnitsyn, A.; Ershova, V.; Khudoley, A.; Shilovskikh, V.; Molchanova, E. Ferro-Manganese Nodules from the Kara Sea: Mineralogy, Geochemistry and Genesis. *Ore Geol. Rev.* **2019**, *106*, 192–204.

(16) Usui, A.; Nishi, K.; Sato, H.; Nakasato, Y.; Thornton, B.; Kashiwabara, T.; Tokumaru, A.; Sakaguchi, A.; Yamaoka, K.; Kato, S.; Nitahara, S.; Suzuki, K.; Iijima, K.; Urabe, T. Continuous Growth of Hydrogenetic Ferromanganese Crusts since 17 Myr Ago on Takuyo-Daigo Seamount, NW Pacific, at Water Depths of 800-5500 m. *Ore Geol. Rev.* **2017**, *87*, 71–87.

(17) Swanner, E.; Planavsky, N.; Lalonde, S.; Robbins, L.; Bekker, A.; Rouxel, O.; Saito, M.; Kappler, A.; Mojzsis, S.; Konhauser, K. Cobalt and Marine Redox Evolution. *Earth Planet. Sci. Lett.* **2014**, *390*, 253–263.

(18) Marino, E.; Gonzalez, F.; Somoza, L.; Lunar, R.; Ortega, L.; Vazquez, J.; Reyes, J.; Bellido, E. Strategic and Rare Elements in Cretaceous-Cenozoic Cobalt-Rich Ferromanganese Crusts from Seamounts in the Canary Island Seamount Province (Northeastern Tropical Atlantic). *Ore Geol. Rev.* **2017**, *87*, 41–61.

(19) Manceau, A.; Gorshkov, A. I.; Drits, V. A. Structural Chemistry of Mn, Fe, Co, and Ni in Mn Hydrous Oxides. II. Information from EXAFS Spectroscopy, Electron and X-Ray Diffraction. *Am. Miner.* **1992**, *77*, 1144–1157.

(20) Manceau, A.; Lanson, M.; Takahashi, Y. Mineralogy and Crystal Chemistry of Mn, Fe, Co, Ni, and Cu in a Deep-Sea Pacific Polymetallic Nodule. *Am. Miner.* **2014**, *99*, 2068–2083.

(21) Usui, A.; Suzuki, K. Geological Characterization of Ferromanganese Crust Deposits in the NW Pacific Seamounts for Prudent Deep-Sea Mining. In *Perspectives on Deep-Sea Mining*; Springer, Cham, 2022; pp 81–113.

(22) Grangeon, S.; Bataillard, P.; Coussy, S. The Nature of Manganese Oxides in Soils and Their Role as Scavengers of Trace Elements: Implications for Soil Remediation. In *Environmental Soil Remediation and Rehabilitation. Applied Environmental Science and Engineering for a Sustainable Future.*; van Hullebusch, E., Huguenot, D., Pechaud, Y., Simonnot, M. O., Colombano, S., Eds.; Springer, Cham, 2020; pp 399–429.

(23) Hein, J. R.; Koschinsky, A. In *Deep-ocean ferromanganese crusts and nodules*; Scott, S., Series Ed.; Treatise on Geochemistry; Elsevier, New York, 2012; pp 273–291.

(24) Murray, J. W. The Interaction of Cobalt with Hydrous Manganese Dioxide. *Geochim. Cosmochim. Acta* **1975**, *39*, 635–647.

(25) Chang, J.; Tani, Y.; Naitou, H.; Miyata, N.; Seyama, H.; Tanaka, K. Cobalt(II) Sequestration on Fungal Biogenic Manganese Oxide Enhanced by Manganese(II) Oxidase Activity. *Appl. Geochem.* **2013**, *37*, 170–178.

(26) Simanova, A. A.; Peña, J. Time-Resolved Investigation of Cobalt Oxidation by Mn(III)-Rich δ-MnO_2 Using Quick X-Ray Absorption Spectroscopy. *Environ. Sci. Technol.* **2015**, *18*, 10867–10876.

(27) Kato, T.; Yu, Q.; Tanaka, K.; Kozai, N.; Saito, T.; Ohnuki, T. Reduction Behaviors of Permanganate by Microbial Cells and Concomitant Accumulation of Divalent Cations of Mg^{2+}, Zn^{2+}, and Co^{2+}. *J. Environ. Sci.* **2019**, *86*, 78–86.

(28) Yin, H.; Liu, F.; Feng, X.; Liu, M.; Tan, W.; Qiu, G. Co^{2+}-Exchange Mechanism of Birnessite and Its Application for the Removal of Pb^{2+} and As(III). *J. Hazard. Mater.* **2011**, *196*, 318–326.

(29) Wang, Y. H.; Benkaddour, S.; Marafatto, F. F.; Pena, J. Diffusion- and pH-Dependent Reactivity of Layer-Type MnO_2: Reactions at Particle Edges versus Vacancy Sites. *Environ. Sci. Technol.* **2018**, *52*, 3476–3485.

(30) Wu, Z. K.; Peacock, C. L.; Lanson, B.; Yin, H.; Zheng, L. R.; Chen, Z. J.; Tan, W. F.; Qiu, G. H.; Liu, F.; Feng, X. H. Transformation of Co-Containing Birnessite to Todorokite: Effect of Co on the Transformation and Implications for Co Mobility. *Geochim. Cosmochim. Acta* **2019**, *246*, 21–40.

(31) Wu, Z.; Lanson, B.; Feng, X.; Yin, H.; Tan, W.; He, F.; Liu, F. Transformation of the Phyllomanganate Vernadite to Tectomanganates with Small Tunnel Sizes: Favorable Geochemical Conditions and Fate of Associated Co. *Geochim. Cosmochim. Acta* **2021**, *295*, 224–236.

(32) Yin, H.; Liu, Y.; Koopal, L. K.; Feng, X. H.; Chu, S. Q.; Zhu, M. Q.; Liu, F. High Co-Doping Promotes the Transition of Birnessite Layer Symmetry from Orthogonal to Hexagonal. *Chem. Geol.* **2015**, *410*, 12–20.

(33) Yin, H.; Li, H.; Wang, Y.; Ginder-Vogel, M.; Qiu, G. H.; Feng, X. H.; Zheng, L. R.; Liu, F. Effects of Co and Ni Co-Doping on the Structure and Reactivity of Hexagonal Birnessite. *Chem. Geol.* **2014**, *381*, 10–20.

(34) McKenzie, R. M. The Reaction of Cobalt with Manganese Dioxide Minerals. *Aust. J. Soil. Res.* **1970**, *8*, 97–106.

(35) Burns, R. G. The Uptake of Cobalt into Ferromanganese Nodules, Soils, and Synthetic Manganese (IV) Oxides. *Geochim. Cosmochim. Acta* **1976**, *40*, 95–102.

(36) McKenzie, R. M. The Adsorption of Lead and Other Heavy Metals on Oxides of Manganese and Iron. *Aust. J. Soil. Res.* **1980**, *18*, 61–73.

(37) Murray, J. W.; Dillard, J. G. The Oxidation of Cobalt(II) Adsorbed on Manganese Dioxide. *Geochim. Cosmochim. Acta* **1979**, *43*, 781–787.

(38) Dillard, J. G.; Crowther, D. L.; Murray, J. W. The Oxidation States of Cobalt and Selected Metals in Pacific Ferromanganese Nodules. *Geochim. Cosmochim. Acta* **1982**, *46*, 755–759.

(39) Crowther, D. L.; Dillard, J. G.; Murray, J. G. The Mechanism of Co(II) Oxidation on Synthetic Birnessite. *Geochim. Cosmochim. Acta* **1983**, *47*, 1399–1403.

(40) Wadsley, A. D. The Crystal Structure of Chalcophanite, $ZnMn_3O_7.3H_2O$. *Acta Cryst.* **1955**, *8*, 1165–1172.

(41) Post, J. E.; Appleman, D. E. Chalcophanite, $ZnMn_3O_7:3H_2O$: New Crystal-Structure Determination. *Am. Miner.* **1988**, *73*, 1401–1404.

(42) Drits, V. A.; Silvester, E.; Gorshkov, A. I.; Manceau, A. Structure of Synthetic Monoclinic Na-Rich Birnessite and Hexagonal Birnessite. Part 1. Results from X-Ray Diffraction and Selected Area Electron Diffraction. *Am. Miner.* **1997**, *82*, 946–961.

(43) Silvester, E.; Manceau, A.; Drits, V. Structure of Synthetic Monoclinic Na-Rich Birnessite and Hexagonal Birnessite .2. Results from Chemical Studies and EXAFS Spectroscopy. *Am. Miner.* **1997**, *82*, 962–978.

(44) Wegorzewski, A. V.; Kuhn, T. The Influence of Suboxic Diagenesis on the Formation of Manganese Nodules in the Clarion Clipperton Nodule Belt of the Pacific Ocean. *Mar. Geol.* **2014**.

(45) Akob, D.; Bohu, T.; Beyer, A.; Schaffner, F.; Handel, M.; Johnson, C.; Merten, D.; Buchel, G.; Totsche, K.; Kusel, K. Identification of Mn(II)-Oxidizing Bacteria from a Low-PH Contaminated Former Uranium Mine. *Appl. Environ. Microbiol.* **2014**, *80*, 5086–5097.

(46) Miyata, N.; Tani, Y.; Sakata, M.; Iwahori, K. Microbial Manganese Oxide Formation and Interaction with Toxic Metal Ions. *J. Biosci. Bioeng.* **2007**, *104*, 1–8.

(47) Saratovsky, I.; Gurr, S. J.; Hayward, M. A. The Structure of Manganese Oxide Formed by the Fungus *Acremonium* Sp Strain KR21-2. *Geochim. Cosmochim. Acta* **2009**, *73*, 3291–3300.

(48) Villalobos, M.; Toner, B.; Bargar, J.; Sposito, G. Characterization of the Manganese Oxide Produced by *Pseudomonas Putida* Strain MnB1. *Geochim. Cosmochim. Acta* **2003**, *67*, 2649–2662.

(49) Tebo, B. M.; Bargar, J. R.; Clement, B. G.; Dick, G. J.; Murray, K. J.; Parker, D.; Verity, R.; Webb, S. M. Biogenic Manganese Oxides: Properties and Mechanisms of Formation. *Annu. Rev. Earth Planet.. Sci.* **2004**, *32*, 287–328.

(50) Grangeon, S.; Lanson, B.; Miyata, N.; Tani, Y.; Manceau, A. Structure of Nanocrystalline Phyllomanganates Produced by Freshwater Fungi. *Am. Miner.* **2010**, *95*, 1608–1616.

(51) Nelson, Y. M.; Lion, L. W.; Ghiorse, W. C.; Shuler, M. L. Production of Biogenic Mn Oxides by *Leprothrix Discophora* SS-1 in a Chemically Defined Growth Medium and Evaluation of Their Pb Adsorption Characteristics. *Appl. Environ. Microbiol.* **1999**, *65*, 175–180.

(52) Frierdich, A.; Catalano, J. G. Distribution and Speciation of Trace Elements in Iron and Manganese Oxide Cave Deposits. *Geochim. Cosmochim. Acta.* **2012**, *91*, 240–253.

(53) Manceau, A.; Kersten, M.; Marcus, M. A.; Geoffroy, N.; Granina, L. Ba and Ni Speciation in a Nodule of Binary Mn Oxide Phase Composition from Lake Baikal. *Geochim. Cosmochim. Acta.* **2007**, *71*, 1967–1981.

(54) Manceau, A.; Lanson, M.; Geoffroy, N. Natural Speciation of Ni, Zn, Ba and As in Ferromanganese Coatings on Quartz Using X-Ray Fluorescence, Absorption, and Diffraction. *Geochim. Cosmochim. Acta* **2007**, *71*, 95–128.

(55) Isaure, M. P.; Manceau, A.; Geoffroy, N.; Laboudigue, A.; Tamura, N.; Marcus, M. A. Zinc Mobility and Speciation in Soil Covered by Contaminated Dredged Sediment Using Micrometer-Scale and Bulk-Averaging X-Ray Fluorescence, Absorption and Diffraction Techniques. *Geochim. Cosmochim. Acta.* **2005**, *69*, 1173-1198.

(56) Bodei, S.; Manceau, A.; Geoffroy, N.; Baronnet, A.; Buatier, M. Formation of Todorokite from Vernadite in Ni-Rich Hemipelagic Sediments. *Geochim. Cosmochim. Acta.* **2007**, *71*, 5698–5716.

(57) Peacock, C. L.; Sherman, D. M. Crystal-Chemistry of Ni in Marine Ferromanganese Crusts and Nodules. *Am. Miner.* **2007**, *92*, 1087–1092.

(58) Takahashi, Y.; Manceau, A.; Geoffroy, N.; Marcus, M. A.; Usui, A. Chemical and Structural Control of the Partitioning of Co, Ce, and Pb in Marine Ferromanganese Oxides. *Geochim. Cosmichim. Acta* **2007**, *71*, 984–1008.

(59) Manceau, A.; Tamura, N.; Celestre, R. S.; MacDowell, A. A.; Geoffroy, N.; Sposito, G.; Padmore, H. A. Molecular-Scale Speciation of Zn and Ni in Soil Ferromanganese Nodules from Loess Soils of the Mississippi Basin. *Environ. Sci. Technol.* **2003**, *37*, 75–80.

(60) Manceau, A.; Marcus, M. A.; Tamura, N.; Proux, O.; Geoffroy, N.; Lanson, B. Natural Speciation of Zn at the Micrometer Scale in a Clayey Soil Using X-Ray Fluorescence, Absorption, and Diffraction. *Geochim. Cosmichim. Acta* **2004**, *68*, 2467–2483.

(61) Manceau, A.; Tommaseo, C.; Rihs, S.; Geoffroy, N.; Chateigner, D.; Schlegel, M.; Tisserand, D.; Marcus, M. A.; Tamura, N.; Chen, Z. S. Natural Speciation of Mn, Ni and Zn at the Micrometer

Scale in a Clayey Paddy Soil Using X-Ray Fluorescence, Absorption, and Diffraction. *Geochim. Cosmochim. Acta.* **2005**, *69*, 4007-4034.

(62) Usui, A.; Mita, N. Geochemistry and Mineralogy of a Modern Buserite Deposit from a Hot Spring in Hokkaido, Japan. *Clays Clay Miner.* **1995**, *43*, 116–127.

(63) McKeown, D. A.; Post, J. E. Characterization of Manganese Oxide Mineralogy in Rock Varnish and Dendrites Using X-Ray Absorption Spectroscopy. *Am. Miner.* **2001**, *86*, 701–713.

(64) Miller, A. Z.; Dionisio, A.; Braga, M. A. S.; Hernandez-Marine, M.; Afonso, M. J.; Muralha, V. S. F.; Herrera, L. K.; Raabe, J.; Fernandez-Cortes, A.; Cuezva, S.; Hermosin, B.; Sanchez-Moral, S.; Chamine, H.; Saiz-Jimenez, C. Biogenic Mn Oxide Minerals Coating in a Subsurface Granite Environment. *Chem. Geol.* **2012**, *322*, 181–191.

(65) Yu, C. X.; Drake, H.; Mathurin, F. A.; Astrom, M. E. Cerium Sequestration and Accumulation in Fractured Crystalline Bedrock: The Role of Mn-Fe (Hydr-)Oxides and Clay Minerals. *Geochim. Cosmochim. Acta* **2017**, *199*, 370–389.

(66) Hochella, M. F.; Kasama, T.; Putnis, A.; Putnis, C. V.; Moore, J. N. Environmentally Important, Poorly Crystalline Fe/Mn Hydrous Oxides: Ferrihydrite and a Possibly New Vernadite-like Mineral from the Clark Fork River Superfund Complex. *Am. Miner.* **2005**, *90*, 718–724.

(67) Tan, H.; Zhang, G.; Heaney, P.; Webb, S.; Burgos, W. Characterization of Manganese Oxide Precipitates from Appalachian Coal Mine Drainage Treatment Systems. *Appl. Geochem.* **2010**, *25*, 389–399.

(68) Usui, A. Nickel and Copper Accumulations as Essential Elements in 10-Å Manganite of Deep-Sea Manganese Nodules. *Nature* **1979**, *279*, 411–413.

(69) Marcus, M. A.; Manceau, A.; Kersten, M. Mn, Fe, Zn and As Speciation in a Fast-Growing Ferromanganese Marine Nodule. *Geochim. Cosmochim. Acta* **2004**, *68*, 3125–3136.

(70) Peacock, C. L.; Moon, E. M. Oxidative Scavenging of Thallium by Birnessite: Explanation for Thallium Enrichment and Stable Isotope Fractionation in Marine Ferromanganese Precipitates. *Geochim. Cosmochim. Acta* **2012**, *84*, 297–313.

(71) Kashiwabara, T.; Oishi, Y.; Sakaguchi, A.; Sugiyama, T.; Usui, A.; Takahashi, Y. Chemical Processes for the Extreme Enrichment of Tellurium into Marine Ferromanganese Oxides. *Geochim. Cosmochim. Acta* **2014**, *131*, 150–163.

(72) Kashiwabara, T.; Takahashi, Y.; Marcus, M.; Uruga, T.; Tanida, H.; Terada, Y.; Usui, A. Tungsten Species in Natural Ferromanganese Oxides Related to Its Different Behavior from Molybdenum in Oxic Ocean. *Geochim. Cosmochim. Acta* **2013**, *106*, 364–378.

(73) Yang, S. T.; Uesugi, S.; Qin, H. B.; Tanaka, M.; Kurisu, M.; Miyamoto, C.; Kashiwabara, T.; Usui, A.; Takahashi, Y. Comparison of Arsenate and Molybdate Speciation in Hydrogenetic Ferromanganese Nodules. *ACS Earth Space Chem.* **2019**, *3*, 29–38.

(74) Lanson, B.; Drits, V. A.; Silvester, E. J.; Manceau, A. Structure of H-Exchanged Hexagonal Birnessite and Its Mechanism of Formation from Na-Rich Monoclinic Buserite at Low PH: New Data from X-Ray Diffraction. *Am. Miner.* **2000**, *85*, 826–835.

(75) Manceau, A.; Drits, V. A.; Silvester, E.; Bartoli, C.; Lanson, B. Structural Mechanism of Co(II) Oxidation by the Phyllomanganate, Na-Buserite. *Am. Miner.* **1997**, *82*, 1150–1175.

(76) Hu, E.; Zhang, Y.; Wu, S.; Wu, J.; Liang, L.; He, F. Role of Dissolved Mn(III) in Transformation of Organic Contaminants: Non-Oxidative versus Oxidative Mechanisms. *Water Res.* **2017**, *111*, 234–243.

(77) Sun, Y.; Im, J.; Shobnam, N.; Fanourakis, S.; He, L.; Anovitz, L.; Erickson, P.; Sun, H.; Zhuang, J.; Loffler, F. Degradation of Adsorbed Bisphenol A by Soluble Mn(III). *Environ. Sci. Technol.* **2021**, *55*, 13014–13023.

(78) Yu, Q.; Sasaki, K.; Tanaka, K.; Ohnuki, T.; Hirajima, T. Structural Factors of Biogenic Birnessite Produced by Fungus *Paraconiothyrium* Sp WL-2 Strain Affecting Sorption of Co^{2+}. *Chem. Geol.* **2012**, *312*, 106–113.

(79) Giovanoli, R. Vernadite Is Random-Stacked Birnessite. *Mineralium Deposita* **1980**, *15*, 251–253.

(80) Manceau, A.; Marcus, M. A.; Grangeon, S.; Lanson, M.; Lanson, B.; Gaillot, A. C.; Skanthakumar, S.; Soderholm, L. Short-Range and Long-Range Order of Phyllomanganate Nanoparticles Determined Using High Energy X-Ray Scattering. *J. Appl. Crystallogr.* **2013**, *46*, 193–209.

(81) Manceau, A.; Steinmann, S. N. Nature of High- and Low-Affinity Metal Surface Sites on Birnessite Nanosheets. *ACS Earth Space Chem.* **2021**, *5*, 66–76.

(82) Elzinga, E. J. Reductive Transformation of Birnessite by Aqueous Mn(II). *Environ. Sci. Technol.* **2011**, *45*, 6366–6372.

(83) Elzinga, E. J.; Kustka, A. B. A Mn-54 Radiotracer Study of Mn Isotope Solid-Liquid Exchange during Reductive Transformation of Vernadite (δ-MnO_2) by Aqueous Mn(II). *Environ. Sci. Technol.* **2015**, *49*, 4310–4316.

(84) Elzinga, E. J. ^{54}Mn Radiotracers Demonstrate Continuous Dissolution and Reprecipitation of Vernadite (δ-MnO_2) during Interaction with Aqueous Mn(II). *Environ. Sci. Technol.* **2016**, *50*, 8670–8677.

(85) Zhao, H. Y.; Zhu, M. Q.; Li, W.; Elzinga, E. J.; Villalobos, M.; Liu, F.; Zhang, J.; Feng, X. H.; Sparks, D. L. Redox Reactions between Mn(II) and Hexagonal Birnessite Change Its Layer Symmetry. *Envirron. Sci. Technol.* **2016**, *50*, 1750–1758.

(86) Wang, Q.; Yang, P.; Zhu, M. Effects of Metal Cations on Coupled Birnessite Structural Transformation and Natural Organic Matter Adsorption and Oxidation. *Geochim. Cosmochim. Acta* **2019**, *250*, 292–310.

(87) Li, Q.; Schild, D.; Pastural, M.; Lützenkirchen, J.; Hanna, K. Alteration of Birnessite Reactivity in Dynamic Anoxic/Oxic. *J. Hazard. Mater.* **2022**, No. 128739.

(88) Neese, F.; Wennmohs, F.; Becker, U.; Riplinger, C. The ORCA Quantum Chemistry Program Package. *J. Chem. Phys.* **2020**, *152*, n° 224108.

(89) Adamo, C.; Barone, V. Toward Reliable Density Functional Methods without Adjustable Parameters: The PBE0 Model. *J. Chem. Phys.* **1999**, *110*, 6158–6170.

(90) Perdew, J. P.; Ernzerhof, M. Rationale for Mixing Exact Exchange with Density Functional Approximations. *J. Chem. Phys.* **1996**, *105*, 9982–9985.

(91) Grimme, S.; Ehrlich, S.; Goerigk, L. Effect of the Damping Function in Dispersion Corrected Density Functional Theory. *J. Comput. Chem.* **2011**, *32*, 1456–1465.

(92) Weigend, F.; Ahlrichs, R. Balanced Basis Sets of Split Valence, Triple Zeta Valence and Quadruple Zeta Valence Quality for H to Rn: Design and Assessment of Accuracy. *Phys. Chem. Chem. Phys.* **2005**, *7*, 3297–3305.

(93) Weigend, F. Accurate Coulomb-Fitting Basis Sets for H to Rn. *Phys. Chem. Chem. Phys.* **2006**, *8*, 1057–1065.

(94) Marenich, A. V.; Cramer, C. J.; Truhlar, D. G. Universal Solvation Model Based on Solute Electron Density and on a Continuum Model of the Solvent Defined by the Bulk Dielectric Constant and Atomic Surface Tensions. *J. Phys. Chem. B* **2009**, *113*, 6378–6396.

(95) Kelly, C. P.; Cramer, C. J.; Truhlar, D. G. Aqueous Solvation Free Energies of Ions and Ion-Water Clusters Based on an Accurate Value for the Absolute Aqueous Solvation Free Energy of the Proton. *J. Phys. Chem. B.* **2006**, *110*, 16066–16081.

(96) Harvey, J.; Aschi, M.; Schwarz, H.; Koch, W. The Singlet and Triplet States of Phenyl Cation. A Hybrid Approach for Locating Minimum Energy Crossing Points between Non-Interacting Potential Energy Surfaces. *Theor. Chem. Acc.* **1998**, *99*, 95–99.

(97) Smith, S. M.; Martell, A. E. *Critical Stability Constants. Vol. 4: Inorganic Complexes*; Plenum Press, 1976.

(98) Burgess, D. R. NIST SRD 46. Critically Selected Stability Constants of Metal Complexes: Version 8.0 for Windows. **2004**, DOI: 10.18434/M32154.

(99) Kwon, K. D.; Refson, K.; Sposito, G. On the Role of Mn(IV) Vacancies in the Photoreductive Dissolution of Hexagonal Birnessite. *Geochim. Cosmochim. Acta* **2009**, *73*, 4142–4150.

(100) Zhao, S.; Wang, Q.; Sun, J.; Borkiewicz, O.; Huang, R.; Saad, E.; Fields, B.; Chen, S.; Zhu, M.; Tang, Y. Effect of Zn Coprecipitation on the Structure of Layered Mn Oxides. *Chem. Geol.* **2018**, *493*, 234–245.

(101) Matocha, C. J.; Elzinga, E. J.; Sparks, D. L. Reactivity of Pb(II) at the Mn(III,IV) (Oxyhydr)Oxide-Water Interface. *Environmental Science and Technology* **2001**, *35*, 2967–2972.

(102) Toner, B.; Manceau, A.; Webb, S. M.; Sposito, G. Zinc Sorption to Biogenic Hexagonal-Birnessite Particles within a Hydrated Bacterial Biofilm. *Geochim. Cosmochim. Acta.* **2006**, *70*, 27–43.

(103) Manceau, A.; Charlet, L. X-Ray Absorption Spectroscopic Study of the Sorption of Cr(III) at the Oxide/Water Interface. I Molecular Mechanism of Cr(III) Oxidation on Mn Oxides. *J. Coll. Interf. Sci.* **1992**, *148*, 443–458.

(104) Peacock, C. L. Physiochemical Controls on the Crystal-Chemistry of Ni in Birnessite: Genetic Implications for Ferromanganese Precipitates. *Geochim. Cosmochim. Acta* **2009**, *73*, 3568–3578.

(105) Manceau, A.; Lanson, B.; Drits, V. A. Structure of Heavy Metal Sorbed Birnessite. Part III. Results from Powder and Polarized Extended X-Ray Absorption Fine Structure Spectroscopy. *Geochim. Cosmochim. Acta.* **2002**, *66*, 2639–2663.

(106) Lanson, B.; Drits, V. A.; Gaillot, A. C.; Silvester, E.; Plançon, A.; Manceau, A. Structure of Heavy Metal Sorbed Birnessite. Part I. Results from X-Ray Diffraction. *Am. Miner.* **2002**, *87*, 1631–1645.

(107) Drits, V. A.; Lanson, B.; Bougerol-Chaillout, C.; Gorshkov, A. I.; Manceau, A. Structure of Heavy Metal Sorbed Birnessite. Part 2. Results from Electron Diffraction. *Am. Miner.* **2002**, *87*, 1646–1661.

(108) Wick, S.; Baeyens, B.; Fernandes, M. M.; Gottlicher, J.; Fischer, M.; Pfenninger, N.; Plotze, M.; Voegelin, A. Thallium Sorption and Speciation in Soils: Role of Micaceous Clay Minerals and Manganese Oxides. *Geochim. Cosmichim. Acta* **2020**, *288*, 83–100.

(109) Cruz-Hernandez, Y.; Villalobos, M.; Marcus, M. A.; Pi-Puig, T.; Zanella, R.; Martinez-Villegas, N. Tl(I) Sorption Behavior on Birnessite and Its Implications for Mineral Structural Changes. *Geochim. Cosmochim. Acta* **2019**, *248*, 356–369.

(110) Kwon, K. D.; Refson, K.; Sposito, G. Surface Complexation of Pb(II) by Hexagonal Birnessite Nanoparticles. *Geochim. Cosmochim. Acta* **2010**, *74*, 6731–6740.

(111) Kwon, K. D.; Refson, K.; Sposito, G. Understanding the Trends in Transition Metal Sorption by Vacancy Sites in Birnessite. *Geochim. Cosmochim. Acta* **2013**, *101*, 222–232.

(112) Grangeon, S.; Lanson, B.; Lanson, M.; Manceau, A. Crystal Structure of Ni-Sorbed Synthetic Vernadite: A Powder X-Ray Diffraction Study. *Min. Mag.* **2008**, *72*, 1197–1209.

(113) Grangeon, S.; Manceau, A.; Guilhermet, J.; Gaillot, A. C.; Lanson, M.; Lanson, L. Zn Sorption Modifies Dynamically the Layer and Interlayer Structure of Vernadite. *Geochim. Cosmochim. Acta* **2012**, *85*, 302–313.

(114) Grangeon, S.; Fernandez-Martinez, A.; Claret, F.; Marty, N.; Tournassat, C.; Warmont, F.; Gloter, A. In-Situ Determination of the Kinetics and Mechanisms of Nickel Adsorption by Nanocrystalline Vernadite. *Chem. Geol.* **2017**, *459*, 24–31.

(115) Yu, Q. Q.; Sasaki, K.; Tanaka, K.; Ohnuki, T.; Hirajima, T. Zinc Sorption During Bio-Oxidation and Precipitation of Manganese Modifies the Layer Stacking of Biogenic Birnessite. *Geomicrobiol. J.* **2013**, *30*, 829–839.

(116) Qin, Z. J.; Xiang, Q. J.; Liu, F.; Xiong, J.; Koopal, L. K.; Zheng, L. R.; Ginder-Vogel, M.; Wang, M. X.; Feng, X. H.; Tan, W. F.; Yin, H. Local Structure of Cu^{2+} in Cu-Doped Hexagonal Turbostratic Birnessite and Cu^{2+} Stability under Acid Treatment. *Chem. Geol.* **2017**, *466*, 512–523.

(117) Zhao, W.; Tan, W.; Feng, X.; Liu, F.; Xie, Y.; Xie, Z. XAFS Studies on Surface Coordination of Pb^{2+} on Birnessites with Different Average Oxidation States. *Coll. Surf. A-Physicochem. Eng. Asp.* **2011**, *379*, 86–92.

(118) Yin, H.; Tan, W.; Zheng, L.; Cui, H.; Qiu, G.; Liu, F.; Feng, X. Characterization of Ni-Rich Hexagonal Birnessite and Its Geochemical Effects on Aqueous Pb^{2+}/Zn^{2+} and As(III). *Geochim. Cosmichim. Acta* **2012**, *93*, 47–62.

(119) van Genuchten, C. M.; Pena, J. Sorption Selectivity of Birnessite Particle Edges: A d-PDF Analysis of Cd(II) and Pb(II) Sorption by δ-MnO_2 and Ferrihydrite. *Environ. Sci-Proc. Imp.* **2016**, *18*, 1030–1041.

(120) Holguera, J. G.; Etui, I. D.; Jensen, L. H. S.; Pena, J. Contaminant Loading and Competitive Access of Pb, Zn and Mn(III) to Vacancy Sites in Biogenic MnO_2. *Chem. Geol.* **2018**, *502*, 76–87.

(121) Yin, H.; Feng, X. H.; Tan, W. F.; Koopal, L. K.; Hu, T. D.; Zhu, M. Q.; Liu, F. Structure and Properties of Vanadium(V)-Doped Hexagonal Turbostratic Birnessite and Its Enhanced Scavenging of Pb^{2+} from Solutions. *J. Hazard. Mater.* **2015**, *288*, 80–88.

(122) Lanson, B.; Marcus, M. A.; Fakra, S.; Panfili, F.; Geoffroy, N.; Manceau, A. Formation of Zn-Ca Phyllomanganate Nanoparticles in Grass Roots. *Geochim. Cosmochim. Acta* **2008**, *72*, 2478–2490.

(123) Tajima, S.; Fuchida, S.; Tokoro, C. Coprecipitation Mechanisms of Zn by Birnessite Formation and Its Mineralogy under Neutral pH Conditions. *J. Environ. Sci.* **2022**, *121*, 136–147.

(124) Kwon, K. D.; Refson, K.; Sposito, G. Defect-Induced Photoconductivity in Layered Manganese Oxides: A Density Functional Theory Study. *Phys. Rev. Lett.* **2008**, *100*, n° 146601.

(125) Lucht, K. P.; Mendoza-Cortes, J. L. Birnessite: A Layered Manganese Oxide To Capture Sunlight for Water-Splitting Catalysis. *J. Phys. Chem. C* **2015**, *119*, 22838–22846.

(126) Wang, C.; Smieszek, N.; Chakrapani, V. Unusually High Electron Affinity Enables the High Oxidizing Power of Layered Birnessite. *Chem. Mater.* **2021**, *33*, 7805–7817.

(127) Weaver, R.; Hochella, M. The Reactivity of Seven Mn-Oxides with Cr^{3+}: A Comparative Analysis of a Complex, Aq Environmentally Important Redox Reaction. *Am. Miner.* **2003**, *88*, 2016–2027.

(128) Smith, P.; Deibert, B.; Kaushik, S.; Gardner, G.; Hwang, S.; Wang, H.; Al-Sharab, J.; Garfunkel, E.; Fabris, L.; Li, J.; Dismukes, G. Coordination Geometry and Oxidation State Requirements of Corner-Sharing MnO_6 Octahedra for Water Oxidation Catalysis: An Investigation of Manganite (γ-MnOOH). *ACS Catalysis* **2016**, *6*, 2089–2099.

(129) Takashima, T.; Hashimoto, K.; Nakamura, R. Mechanisms of PH-Dependent Activity for Water Oxidation to Molecular Oxygen by MnO_2 Electrocatalyst. *J. Am. Chem. Soc.* **2012**, *134*, 1519–1527.

(130) Chan, Z.; Kitchaev, D.; Weker, J.; Schnedermann, C.; Lim, K.; Ceder, G.; Tumas, W.; Toney, M.; Nocera, D. Electrochemical Trapping of Metastable Mn^{3+} Ions for Activation of MnO_2 Oxygen Evolution Catalysts. *Proc. Natl. Acad. Sci. U. S. A.* **2018**, *115*, E5261–E5268.

(131) Peng, H.; McKendry, I.; Ding, R.; Thenuwara, A.; Kang, Q.; Shumlas, S.; Strongin, D.; Zdilla, M.; Perdew, J. Redox Properties of Birnessite from a Defect Perspective. *Proc. Natl. Acad. Sci. U. S. A.* **2017**, *114*, 9523–9528.

(132) Peacock, C. L.; Sherman, D. M. Sorption of Ni by Birnessite: Equilibrium Controls on Ni in Seawater. *Chem. Geol.* **2007**, *238*, 94–106.

(133) Moore, E. A.; Janes, R. *Metal-Ligand Bonding*; Royal Soc. Chem., 2004.

(134) Shannon, R. D. Revised Effective Ionic Radius and Systematic Studies of Interatomic Distances in Halides and Chalcogenides. *Acta Crystallographica* **1976**, *B25*, 925–946.

(135) Goodwin, H. A. Spin Crossover in Cobalt(II) Systems. *Top Curr. Chem.* **2004**, *234*, 23–47.

(136) Zhu, M. Q.; Ginder-Vogel, M.; Parikh, S. J.; Feng, X. H.; Sparks, D. L. Cation Effects on the Layer Structure of Biogenic Mn-Oxides. *Environ. Sci. Technol.* **2010**, *44*, 4465–4471.

(137) Lefkowitz, J. P.; Elzinga, E. J. Impacts of Aqueous Mn(II) on the Sorption of Zn(II) by Hexagonal Birnessite. *Environ. Sci. Technol.* **2015**, *49*, 4886–4893.

(138) van Leest, N.; de Bruin, B. Revisiting the Electronic Structure of Cobalt Porphyrin Nitrene and Carbene Radicals with NEVPT2-CASSCF Calculations: Doublet versus Quartet Ground States. *Inorg. Chem.* **2021**, *60*, 8380–8387.

(139) Zhong, Y.; Xu, X.; Veder, J.; Shao, Z. Self-Recovery Chemistry and Cobalt-Catalyzed Electrochemical Deposition of Cathode for Boosting Performance of Aqueous Zinc-Ion Batteries. *IScience* **2020**, *23*, n° 100943.

(140) Lahtinen, K.; Labmayr, M.; Mäkelä, V.; Jiang, H.; Lahtinen, J.; Yao, L.; Fedorovskaya, E. O.; Räsänen, S.; Huotari, S.; Kallio, T. Long Term Cycling Behavior of Mg-Doped $LiCoO_2$ Materials Investigated with the Help of Laboratory Scale X-Ray Absorption near-Edge Spectroscopy. *Mater. Today Energy* **2022**, in press.

(141) Yang, S.; Zhang, L.; Luo, M.; Cui, Y.; Wang, J.; Zhao, D.; Yang, C.; Wang, X.; Cao, B. Synergistic Combination of a Co-Doped σ-MnO_2 Cathode with an Electrolyte Additive for a High-Performance Aqueous Zinc-Ion Battery. *Chem. Phys. Mater.* **2022**, in press.

(142) Biswal, A.; Minakshi, M.; Tripathy, B. Electrodeposition of Sea Urchin and Cauliflower-like Nickel-/Cobalt-Doped Manganese Dioxide Hierarchical Nanostructures with Improved Energy-Storage Behavior. *Chem. Electro. Chem.* **2016**, *3*, 976–985.

(143) Pu, X.; Ren, X.; Yin, H.; Tang, Y.; Yuan, H. One-Step Electrodeposition Strategy for Growing Nickel Cobalt Hydroxysulfide Nanosheets for Supercapacitor Application. *J. Alloys Compd.* **2021**, *865*, n° 158736.

(144) Moon, J.; Nulu, A.; Hwang, Y.; Nulu, V.; Sohn, K. Facile Synthesis of Porous Hollow Cobalt-Doped λ-MnO_2 Nano Architectures as a High-Performance Anode Material for Li-Ion Batteries and Li-Ion Hybrid Supercapacitors. *ChemistrySelect* **2021**, *6*, 7012–7024.

(145) Chen, L.; Ding, J.; Jia, J.; Ran, R.; Zhang, C.; Song, X. Cobalt-Doped MnO_2 Nanofibers for Enhanced Propane Oxidation. *ACS Appl. Nano Mater.* **2019**, *2*, 4417–4426.

(146) Li, G.; Li, N.; Sun, Y.; Qu, Y.; Jiang, Z.; Zhao, Z.; Zhang, Z.; Cheng, J.; Hao, Z. Efficient Defect Engineering in Co-Mn Binary Oxides for Low-Temperature Propane Oxidation. *Appl. Catal.* **2021**, *282*, n° 119512.

(147) Song, M.; Tan, H.; Chao, D.; Fan, H. Recent Advances in Zn-Ion Batteries. *Adv. Funct. Mater.* **2018**, *28*, n° 1802564.

(148) Wu, B.; Zhang, G.; Yan, M.; Xiong, T.; He, P.; He, L.; Xu, X.; Mai, L. Graphene Scroll-Coated α-MnO_2 Nanowires as High-Performance Cathode Materials for Aqueous Zn-Ion Battery. *Small* **2018**, *14*, n° 1703850.

(149) Cheng, F.; Zhang, T.; Zhang, Y.; Du, J.; Han, X.; Chen, J. Enhancing Electrocatalytic Oxygen Reduction on MnO_2 with Vacancies. *Angew. Chem. Int. Ed.* **2013**, *52*, 2474–2477.

(150) Zhao, Y.; Chang, C.; Teng, F.; Zhao, Y.; Chen, G.; Shi, R.; Waterhouse, G.; Huang, W.; Zhang, T. Defect-Engineered Ultrathin δ-MnO_2 Nanosheet Arrays as Bifunctional Electrodes for Efficient Overall Water Splitting. *Adv. Energ. Mater.* **2017**, *7*, n° 1700005.

FIGURE CAPTION

Figure. 1. Polyhedral representation of Co-birnessite surface complexes. (a) triple-corner-sharing (TCS) complex wherein a [Co(II)O_6] octahedron binds to the three doubly-coordinated oxygen atoms (O_{2Mn}) surrounding a vacancy site of the MnO_2 layer. (b) Incorporation (INC) of Co(III) into a vacancy. (c) Double-edge-sharing (DES) complex wherein a [Co(II)O_6] octahedron binds to two singly- and one doubly-coordinated oxygen atoms at the layer edge. (d) Triple-edge-sharing (TES) complex wherein a [Co(II)O_6] octahedron binds to two singly- and two doubly-coordinated oxygen atoms at the layer edge. (e) Double-corner-sharing (DCS) complex wherein a [Co(II)O_6] octahedron binds to two singly-coordinated oxygen atoms at the layer edge. Mn(IV) octahedron = gray; Co(II) octahedron = cyan; Co(III) octahedron = blue; oxygen = red, proton = gray.

Figure 2. Polyhedral representation of the four Mn_9V-type nanolayers used to model the oxidation of Co(II) on basal surfaces. (a) Nanolayer 1, $Mn^{3+}_{Layer}Mn_8V$. (b) Nanolayer 2, $Mn^{3+}_{TCS}Mn_9V$. (c) Nanolayer 3, Mn_9V. (d) Nanolayer 4, $Mn^{3+\downarrow}_{TCS}Mn^{3+\uparrow}_{Layer}Mn_8V$. Mn(IV) octahedron = gray; Mn(III) octahedron = purple; oxygen = red, proton = gray.

Figure 3. Schematic pathways of reaction 1. Co(II) adsorbs as a TCS complex at a vacancy site, and is oxidized as an INC complex by an adjacent Mn(III) in the layer. Reduced Mn(II) forms a TCS complex in pathway 1a, and is released to solution in pathway 1b. Mn(IV) octahedron = gray; Mn(III) octahedron = purple; Mn(II) octahedron = dark red; Co(II) octahedron = cyan; Co(III) octahedron = blue; oxygen = red, proton = gray.

Figure 4. Schematic pathways of reaction 2. Mn(III) from a Mn(III)-TCS complex reacts with a hexahydrated Co^{2+} ion (a). Co(II) is oxidized by Mn(III), which is reduced to hexahydrated Mn^{2+} (pathway 2a) (b). Afterward, Co(III) fills the vacancy site (Pathway 2b) (c). Mn(IV) octahedron = gray; Mn(III) octahedron = purple; Co(III) octahedron = blue; oxygen = red, proton = gray.

Figure 5. Schematic pathways of reactions 4 and 5. In reaction 4, Co(II) adsorbs as a TCS complex at a vacancy site (a), and is oxidized as an INC complex by an adjacent Mn(IV) in the layer. The two undersaturated oxygens bonded to Mn(IV), Mn(III) and Co(III) are deprotonated in pathway 4a (b), and protonated in pathway 4b (c). Reaction 5 involves the disproportionation of a $Mn^{3+\downarrow}_{TCS}Mn^{3+\uparrow}_{Layer}$ pair (d) by a Co(II)-TCS complex (a), which is subsequently oxidized to a Co(III)-INC complex through reaction 4. Mn(IV) octahedron = gray; Mn(III) octahedron = purple; Co(II) octahedron = cyan; Co(III) octahedron = blue; oxygen = red, proton = gray.

Figure 6. Releaxed potential energy surface (PES) scan of the migration of Co(II) and Ni(II) into a deprotonated Mn(IV) vacancy site. The torsion angle is defined as a dihedral angle between Co/Ni and three Mn atoms. The two reactants (R) are an octahedral TCS complex ($Me^{2+}_{TCS}Mn^{4+}_{9}V_d$) over a fully deprotonated vacancy (V_d) and the two products (P) are an INC complex ($Me^{2+}_{INC}Mn^{4+}_{9}$). The intermediate product (IP1) is a tetrahedral complex over the vacancy site ($^{IV}Me^{2+}_{TCS}Mn^{4+}_{9}$). The oxidation and spin states of Co cannot be changed during a PES scan, and therefore the variation of the electronic energy (ΔE = -11.2 kcal/mol) is higher than when Co(II) is oxidized to Co(III).

Figure 7. Energetic span model of the oxidation of Co(II) to Co(III) on deprotonated Mn(IV) vacancy sites in birnessite. Co initially forms an octahedral $Co^{2+}_{TCS}Mn^{4+}_{9}V_d$ complex (reactant, R) and goes through transition state TS1 to reach the intermediate product (IP1), in which Co(II) is tetrahedrally

coordinated ($^{IV}Co^{2+}_{TCS}Mn^{4+}_{9}V_{d}$ complex). The potential electronic energy of TS1 is $\Delta E^{\ddagger}$ = 7.2 kcal/mol higher than that of R ($\Delta G^{\ddagger}$ = 4.4 kcal/mol). IP1 is as stable as R (ΔE = 1.5 kcal/mol, ΔG = -0.4 kcal/mol, reaction 7a, Table 1). When the vacancy is protonated, ΔE(IP1) = 5.5 kcal/mol and ΔG(IP1) = 4.2 kcal/mol relative to R (reaction 7b). Then, IP1 surmounts a potential activation barrier of 3.0 kcal/mol ($\Delta G^{\ddagger}$ = 2.4 kcal/mol) to form a second intermediate product (IP2), in which Co(II) is in low-spin state ($t_{2g}^{6}e_{g}^{1}$) and occupies the center of the vacancy ($^{VI}Co^{2+,LS}_{INC}Mn^{4+}_{9}$ complex). IP2 is also as stable as R (ΔE = 1.7 kcal/mol, ΔG = 0.1 kcal/mol , reaction 8). Finally, the e_g electron of Co(II) is transferred to a Mn^{4+} ion to form the reaction product (P, $Co^{3+}_{INC}Mn^{3+}_{Layer}Mn^{4+}_{8}$ complex, ΔE = -16.4 kcal/mol and ΔG = -17.6 kcal/mol relative to R, reaction 6, Figure S2). When the vacancy of the reactant is protonated, protons are likely released in the course of the migration of the $^{IV}Co^{2+}$ ion into the empty Mn^{4+} site. Mn(IV) octahedron = gray; Mn(III) octahedron = purple; high-spin Co(II) octahedron = cyan; low-spin Co(II) octahedron = light blue; Co(III) octahedron = blue; oxygen = red, proton = gray.

Figure 8. Polyhedral representation of the $Mn^{3+}Mn^{4+}_{6}$ (a) , and Mn^{4+}_{7} (b), nanolayers used to model the oxidation of Co(II) on lateral surfaces. Mn(IV) octahedron = gray; Mn(III) octahedron = purple; oxygen = red, proton = gray.

Figure 9. Schematic pathways of reactions 3, 9 and 10. In reaction 3, Co(II) adsorbs as a DCS complex on a nanolayer edge, is oxidized by an adjacent Mn(III) in the layer and replaces reduced Mn(II), which is released to solution (a). In reaction 9, a Co(II)-DCS complex is oxidized by a an adjacent Mn(IV) in the layer and forms a Co(III)-DES complex (b). In reaction 10, Co(II) adsorbs as a DES complex and is oxidzed to a Co(III)-DES complex by an adjacent Mn(IV) in the layer (c). Mn(IV) octahedron = gray; Mn(III) octahedron = purple; Co(II) octahedron = cyan; Co(III) octahedron = blue; oxygen = red, proton = gray.

Table 1. Gibbs free energy change (ΔG in kcal/mol) and ratio of the concentrations of the Co(III) and Co(II) complexes at pH 4 and 7 for all oxidation reactions modeled by DFT.

ID	Nanolayer	Chemical reaction	ΔG	[P]/[R], pH4	[P]/[R], pH7
1a	$Mn^{3+}_{Layer}Mn^{4+}_{8}V$	$Co^{2+}_{TCS}Mn^{3+}_{Layer} \rightarrow Co^{3+}_{INC} + Mn^{2+}_{TCS}$	4.4	5.9×10^{-4}	5.9×10^{-4}
1b	$Mn^{3+}_{Layer}Mn^{4+}_{8}V$	$Co^{2+}_{TCS}Mn^{3+}_{Layer} + 2H^{+} + 3H_2O \rightarrow Co^{3+}_{INC} + Mn^{2+}_{sol}$	4.2	8.3×10^{-12}	8.3×10^{-18}
2a	$Mn^{3+}_{TCS}Mn^{4+}_{9}V$	$Co^{2+}_{sol} + Mn^{3+}_{TCS} \rightarrow Co^{3+}_{TCS} + Mn^{2+}_{sol}$	17.1	2.9×10^{-13}	2.9×10^{-13}
2b	$Mn^{3+}_{TCS}Mn^{4+}_{9}V$	$Co^{3+}_{TCS} \rightarrow Co^{3+}_{INC} + 2H^{+} + 3H_2O$	-17.7	9.4×10^{20}	9.4×10^{26}
3	$Mn^{3+}_{Layer}Mn^{4+}_{6}$	$Co^{2+}_{DCS}Mn^{3+}_{Layer} + 3H_2O \rightarrow Co^{3+}_{TES} + Mn^{2+}_{sol}$	34.1	1.0×10^{-25}	1.0×10^{-25}
4a	$Mn^{4+}_{9}V$	$Co^{2+}_{TCS}Mn^{4+}_{Layer} \rightarrow Co^{3+}_{INC}Mn^{3+}_{Layer} + 2H^{+} + 3H_2O$	16.9	4.1×10^{-5}	40.9
4b	$Mn^{4+}_{9}V$	$Co^{2+}_{TCS}Mn^{4+}_{Layer} \rightarrow Co^{3+}_{INC}Mn^{3+}_{Layer} 2H^{+} + 3H_2O$	-5.2	6.5×10^{3}	6.5×10^{3}
5	$Mn^{3+\downarrow}_{TCS}Mn^{3+\uparrow}_{Layer}Mn^{4+}_{8}V$	$Co^{2+}_{sol} + Mn^{3+\downarrow}_{TCS}Mn^{3+\uparrow}_{Layer} \rightarrow Co^{2+}_{TCS}Mn^{4+}_{Layer} + Mn^{2+}_{sol}$	-6.7	8.1×10^{4}	8.1×10^{4}
5	$Mn^{3+\downarrow}_{TCS}Mn^{3+\uparrow}_{Layer}Mn^{4+}_{22}V$	$Co^{2+}_{sol} + Mn^{3+\downarrow}_{TCS}Mn^{3+\uparrow}_{Layer} \rightarrow Co^{2+}_{TCS}Mn^{4+}_{Layer} + Mn^{2+}_{sol}$	-6.3	4.1×10^{4}	4.1×10^{4}
6	$Mn^{4+}_{9}V_d$	$Co^{2+}_{TCS}Mn^{4+}_{Layer} \rightarrow Co^{3+}_{INC}Mn^{3+}_{Layer}$	-17.6	8.0×10^{12}	8.0×10^{12}
7a	$Mn^{4+}_{9}V_d$	$Co^{2+}_{TCS}Mn^{4+}_{Layer} \rightarrow {}^{IV}Co^{2+}_{TCS}Mn^{4+}_{Layer}$	-0.4	2.0	2.0
7b	$Mn^{4+}_{9}V$	$Co^{2+}_{TCS}Mn^{4+}_{Layer} \rightarrow {}^{IV}Co^{2+}_{TCS}Mn^{4+}_{Layer}$	4.2	8.3×10^{-4}	8.3×10^{-4}
8	$Mn^{4+}_{9}V_d$	$Co^{2+}_{TCS}Mn^{4+}_{Layer} \rightarrow Co^{2+,LS}_{INC}Mn^{4+}_{Layer}$	0.1	1.0	1.0
9	Mn^{4+}_{7}	$Co^{2+}_{DCS}Mn^{4+}_{Layer} \rightarrow Co^{3+}_{DES}Mn^{3+}_{Layer} + H^{+} + 3H_2O$	19.5	5.1×10^{-11}	5.1×10^{-8}
10	Mn^{4+}_{7}	$Co^{2+}_{DES}Mn^{4+}_{Layer} \rightarrow Co^{3+}_{DES}Mn^{3+}_{Layer}$	21.1	3.4×10^{-16}	3.4×10^{-16}

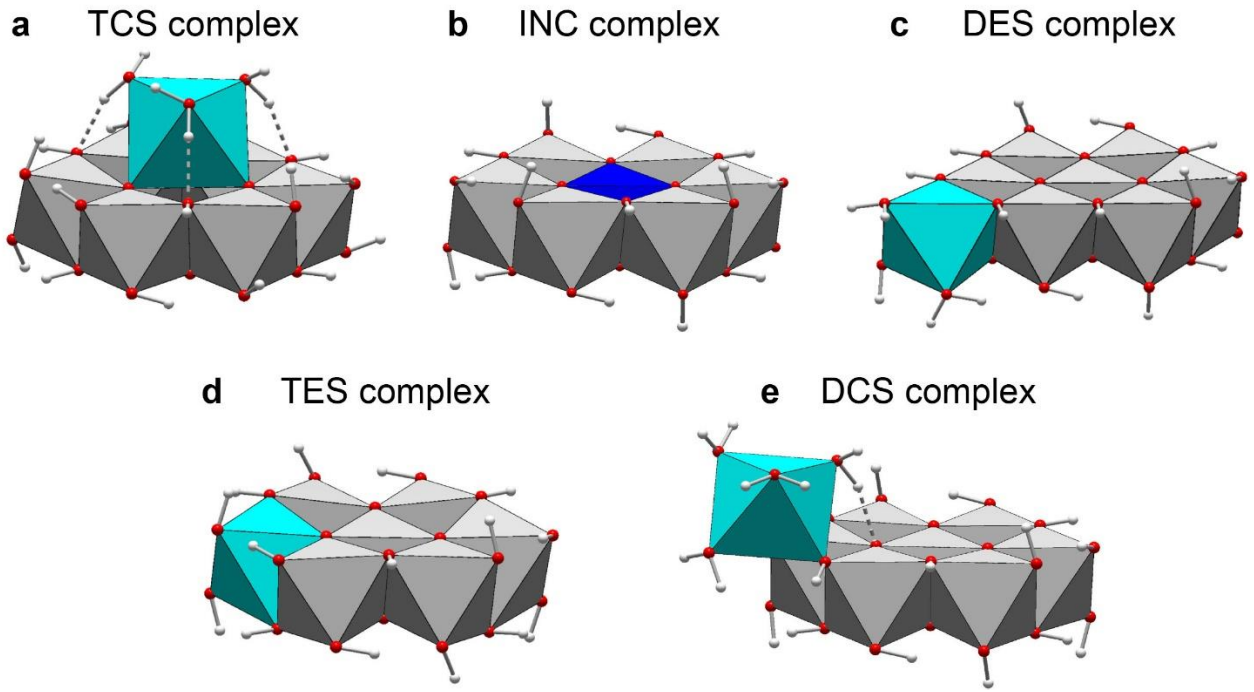

Figure 1

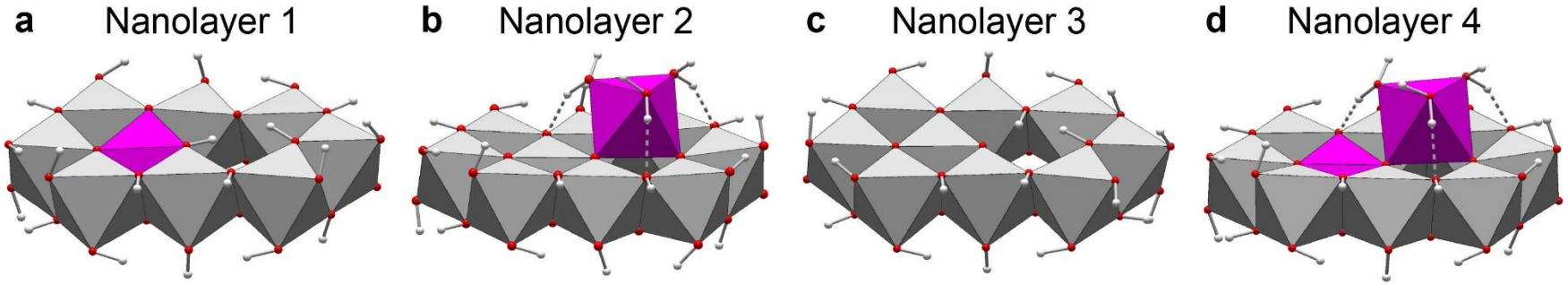

Figure 2

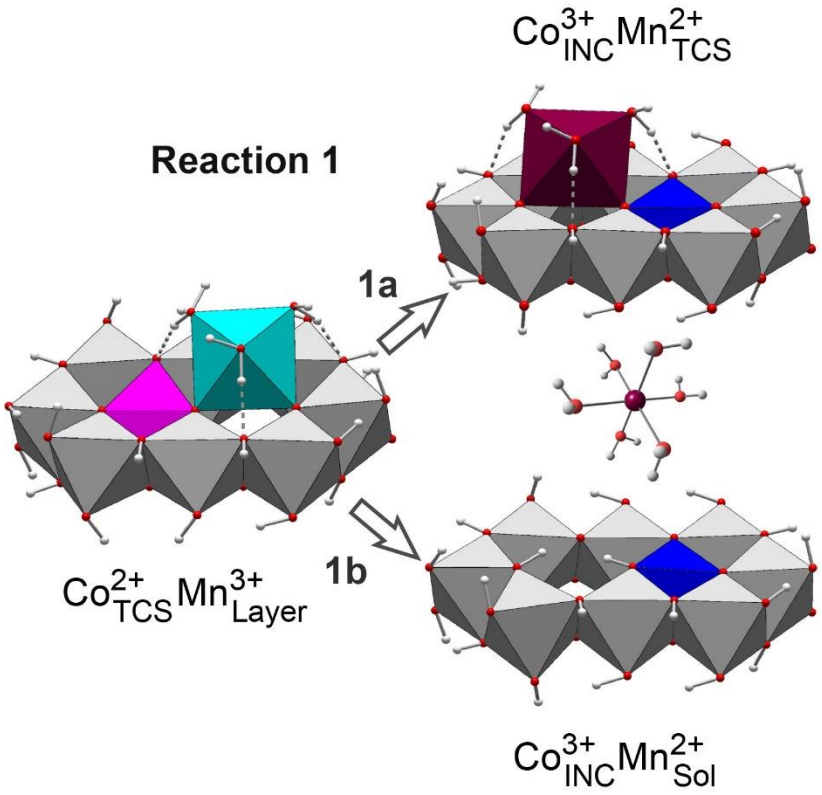
Reaction 1
$Co^{3+}_{INC}Mn^{2+}_{TCS}$
1a
$Co^{2+}_{TCS}Mn^{3+}_{Layer}$
1b
$Co^{3+}_{INC}Mn^{2+}_{Sol}$

Figure 3

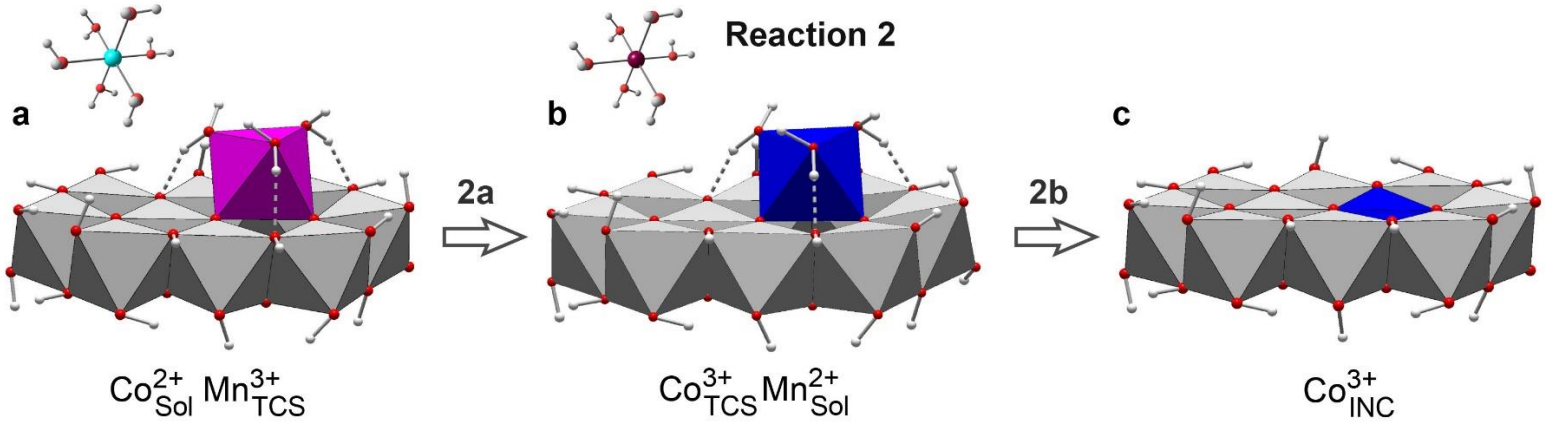

Figure 4

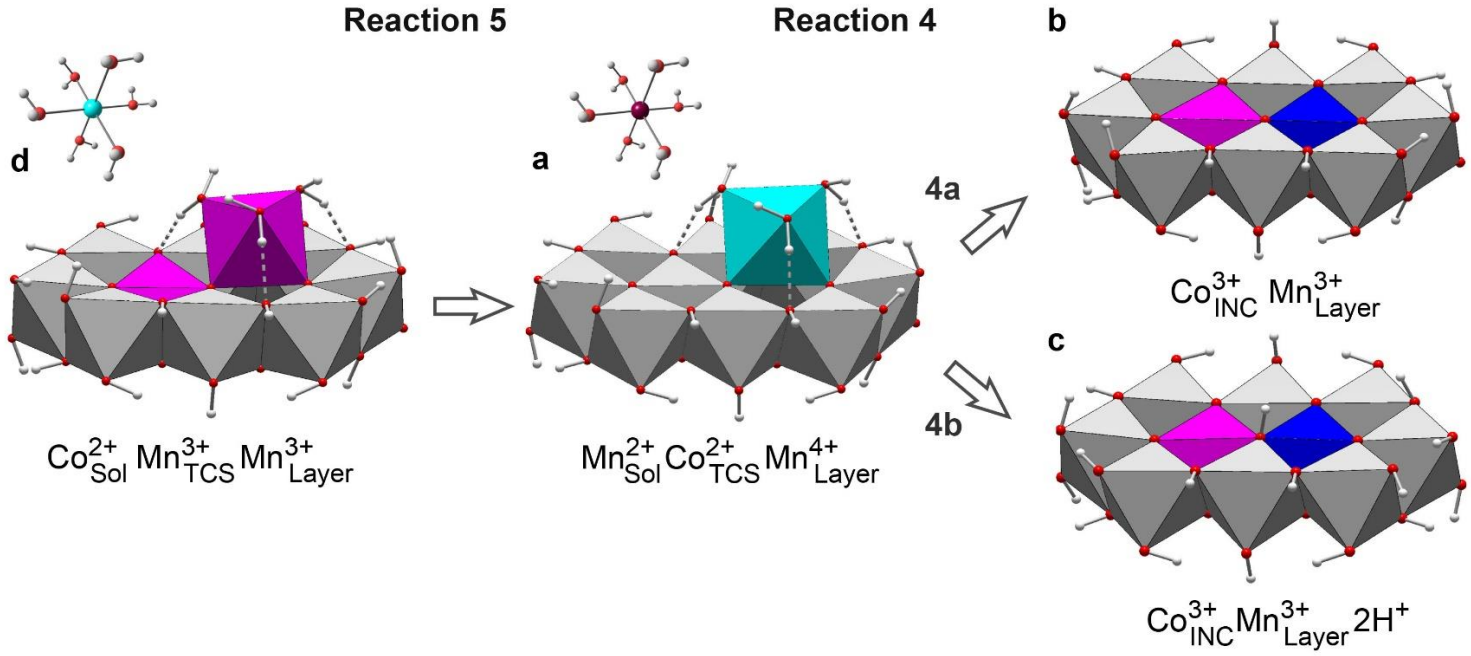

Figure 5

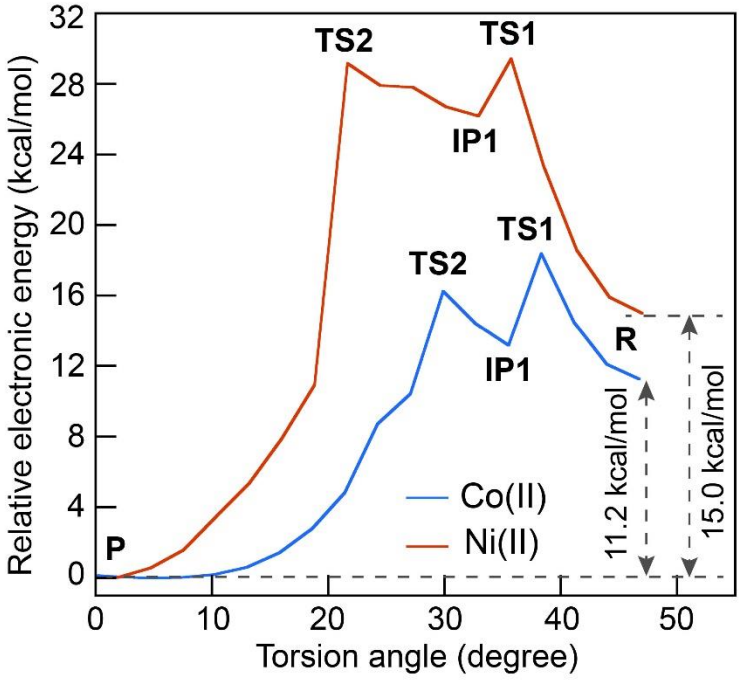
Relative electronic energy (kcal/mol)
Torsion angle (degree)
TS2
TS1
IP1
TS1
TS2
IP1
R
P
Co(II)
Ni(II)
11.2 kcal/mol
15.0 kcal/mol
0
4
8
12
16
20
24
28
32
0
10
20
30
40
50

Figure 6

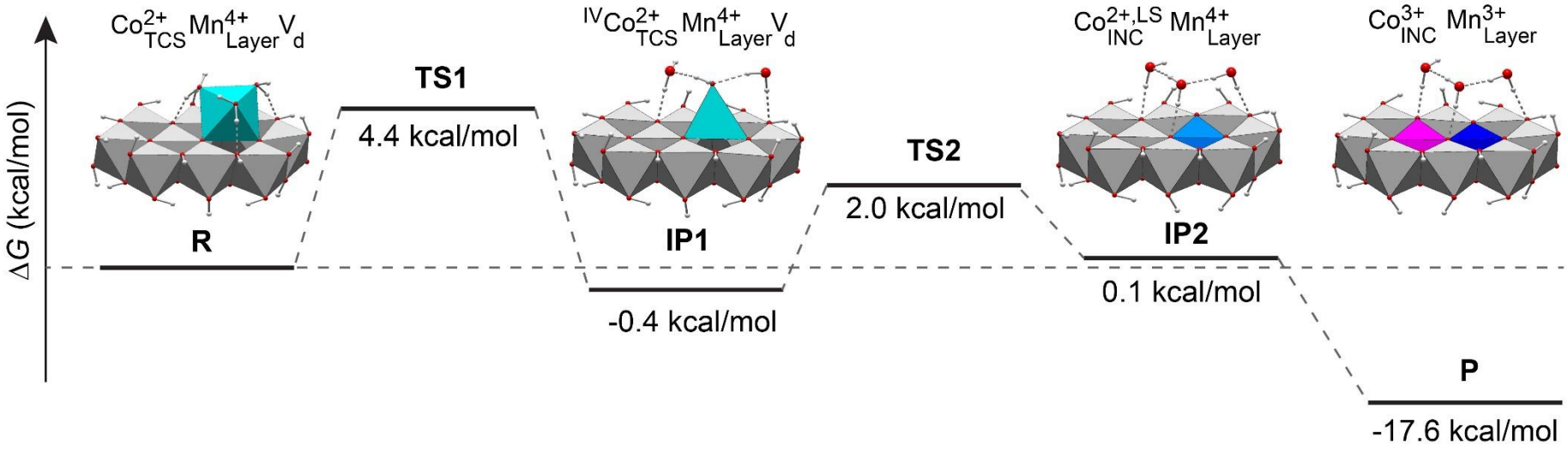
ΔG (kcal/mol)
Co2+TCS Mn4+Layer Vd
R
TS1
4.4 kcal/mol
IVCo2+TCS Mn4+Layer Vd
IP1
-0.4 kcal/mol
TS2
2.0 kcal/mol
Co2+,LSINC Mn4+Layer
IP2
0.1 kcal/mol
Co3+INC Mn3+Layer
P
-17.6 kcal/mol

Figure 7

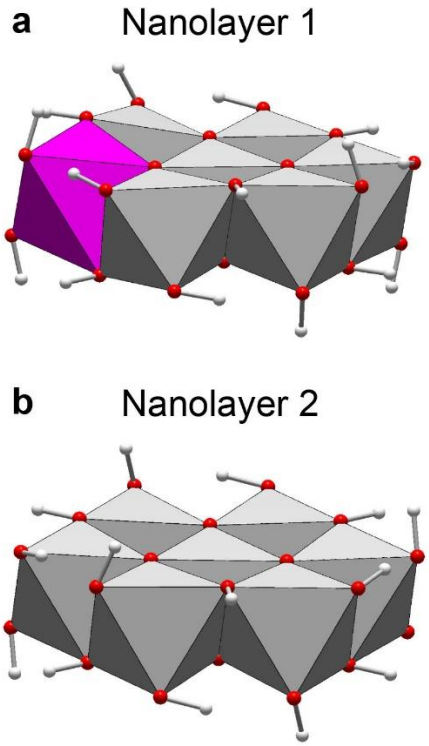

Figure 8

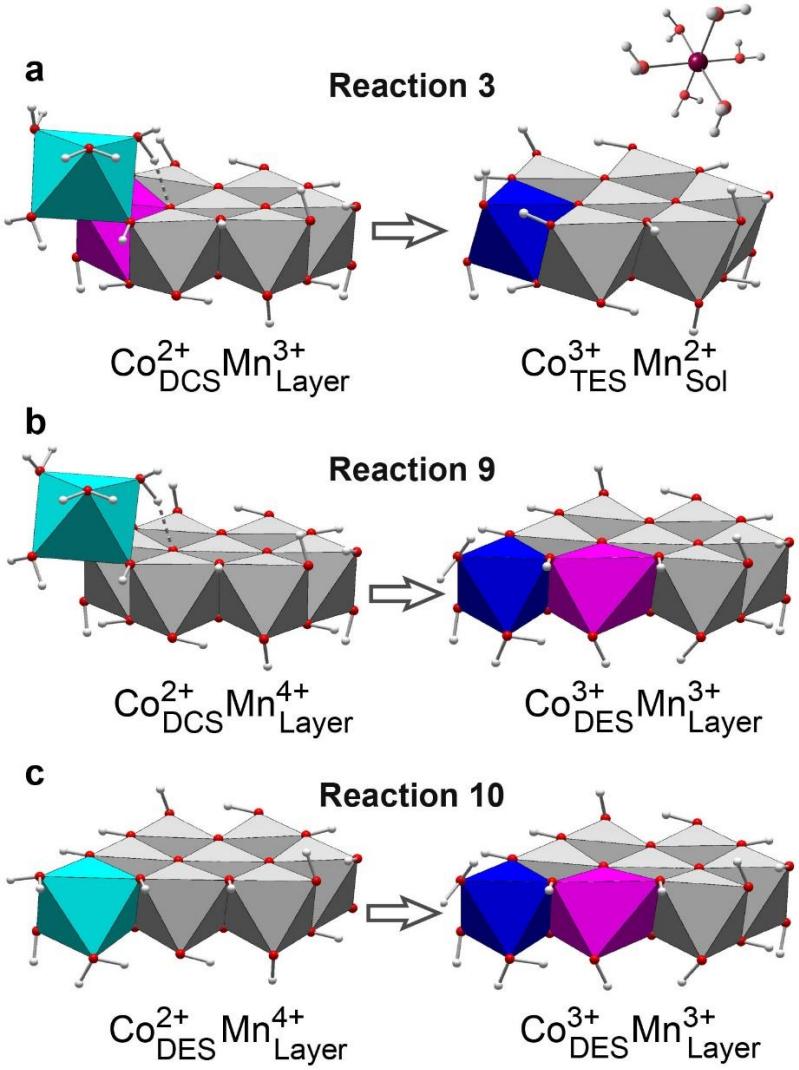
a
Reaction 3
$Co^{2+}_{DCS}Mn^{3+}_{Layer}$
$Co^{3+}_{TES}Mn^{2+}_{Sol}$
b
Reaction 9
$Co^{2+}_{DCS}Mn^{4+}_{Layer}$
$Co^{3+}_{DES}Mn^{3+}_{Layer}$
c
Reaction 10
$Co^{2+}_{DES}Mn^{4+}_{Layer}$
$Co^{3+}_{DES}Mn^{3+}_{Layer}$

Figure 9

Supplementary Information

Density Functional Theory Modeling of the Oxidation Mechanism of Co(II) by Birnessite

Alain Manceau[*a] and Stephan N. Steinmann[b]

[a] Univ. Grenoble Alpes, CNRS, ISTerre, CS 40700, 38058 Grenoble, France

[b] ENS de Lyon, CNRS, Laboratoire de Chimie, 69342 Lyon, France

Corresponding Author :

alain.manceau@univ-grenoble-alpes.fr

Supplementary Table

Table S1. Total electronic charge, Mulliken atomic spin density (ρ), and multiplicity of the complexes

Figure	Complex	Charge	Spin density	Multiplicity
3	$Co^{2+}_{TCS}Mn^{3+}_{Layer}$	-3	Co : 2.81 Mn: 3.97	32
3	$Co^{3+}_{INC}Mn^{2+}_{TCS}$	-3	Co: 0.02 Mn: 4.91	30
3	$Co^{3+}_{INC}V$	-3	Co: -0.01	25
4	Mn^{3+}_{TCS}	-1	Mn: 4.02	32
4	Co^{3+}_{TCS}	-1	Co: 0.04	28
4	Co^{3+}_{INC}	-3	Co: 1.95	28
5	$Mn^{3+}_{TCS}Mn^{3+}_{Layer}$	-2	Mn: 3.97 Mn: 4.04	33
5, S2	$Co^{2+}_{TCS}Mn^{4+}_{Layer}$	-2	Co: 2.81	31
5	$Co^{3+}_{INC}Mn^{3+}_{Layer}$	-4	Co: 0.00 Mn: 3.93	29
5	$Co^{3+}_{INC}Mn^{3+}_{Layer}2H^{+}$	-2	Co: 0.00 Mn: 3.94	29
7, S2	$Co^{2+}_{TCS}Mn^{4+}_{Layer}V_d$	-4	Co: 2.81	31
7, S2	$^{IV}Co^{2+}_{TCS}Mn^{4+}_{Layer}V_d$	-4	Co: 2.82	31
7, S2	$Co^{2+,LS}_{INC}Mn^{4+}_{Layer}$	-4	Co: 0.96	29
7, S2	$Co^{3+}_{INC}Mn^{3+}_{Layer}$	-4	Co: 0.00 Mn: 3.95	29
9	$Co^{2+}_{DCS}Mn^{3+}_{Layer}$	-1	Co: 2.81 Mn: 4.02	26

9	Co^{3+}_{TES}	-3	Co: 0.02	19
9	$Co^{2+}_{DCS}Mn^{4+}_{Layer}$	0	Co: 2.81	25
9	$Co^{3+}_{DES}Mn^{3+}_{Layer}$	-1	Co: 0.02 Mn: 4.00	23
9	$Co^{2+}_{DES}Mn^{4+}_{Layer}$	-1	Co: 2.81	25
S2	$^{IV}Co^{2+}_{TCS}Mn^{4+}_{Layer}$	-2	Co: 2.82	31

Supplementary figures

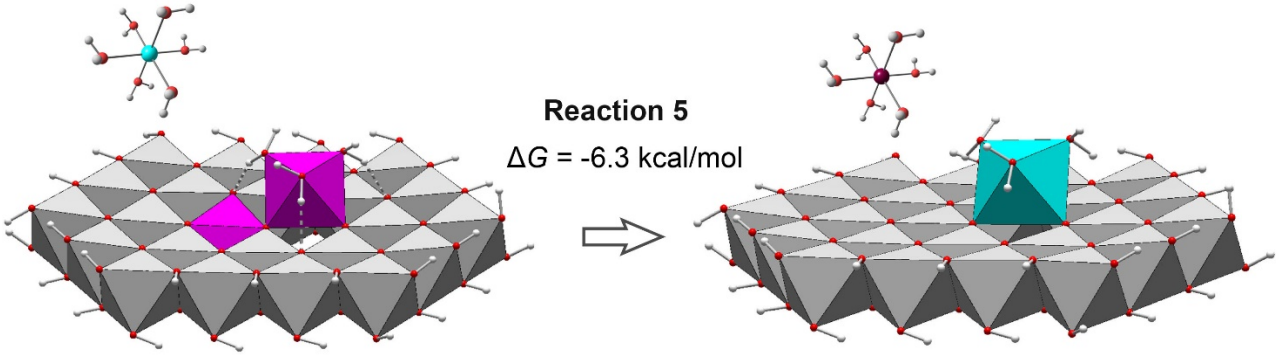

Figure S1. Schematic pathway and Gibbs free-energy (ΔG) of reaction 5 (Figure 5) for a $Mn_{23}V$ nanolayer. Mn(IV) octahedron = gray; Mn(III) octahedron = purple; Co(II) octahedron = cyan; Co(III) octahedron = blue; oxygen = red, proton = gray.

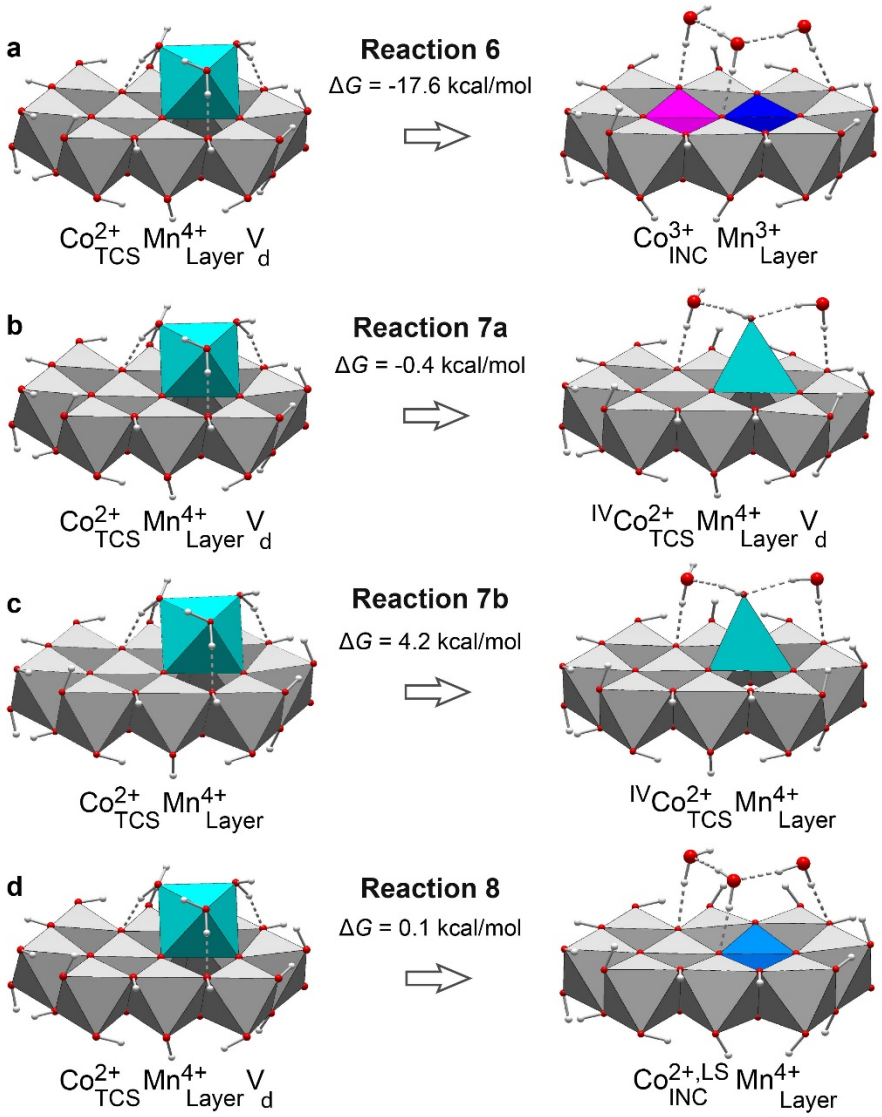

Figure S2. Schematic pathways and Gibbs free-energies of complexation (ΔG) of reactions 6, 7a, 7b, and 8. Mn(IV) octahedron = gray; Mn(III) octahedron = purple; high-spin Co(II) octahedron = cyan; low-spin Co(II) octahedron = light blue; Co(III) octahedron = blue; oxygen = red, proton = gray.

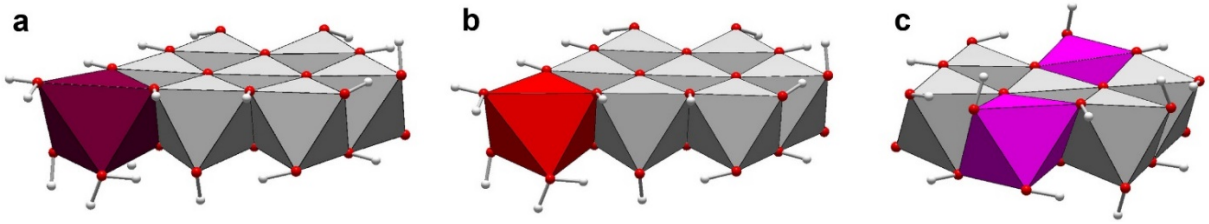

Figure S3. Geometry-optimized ferromagnetic Mn(II)-DES complex (G = -7060297.1 kcal/mol) (a), antiferromagnetic Mn(II)-DES complex (G = -7060297.4 kcal/mol) (b), and ferromagnetic Mn(II)-TES complex (c), at the layer edge. The two DES complexes are stable and the TES complex undergoes comproportionation with a layer Mn(IV). Mn(IV) octahedron = gray; Mn(III) octahedron = purple; Mn(II) octahedron = dark and bright red; oxygen = red, proton = gray.

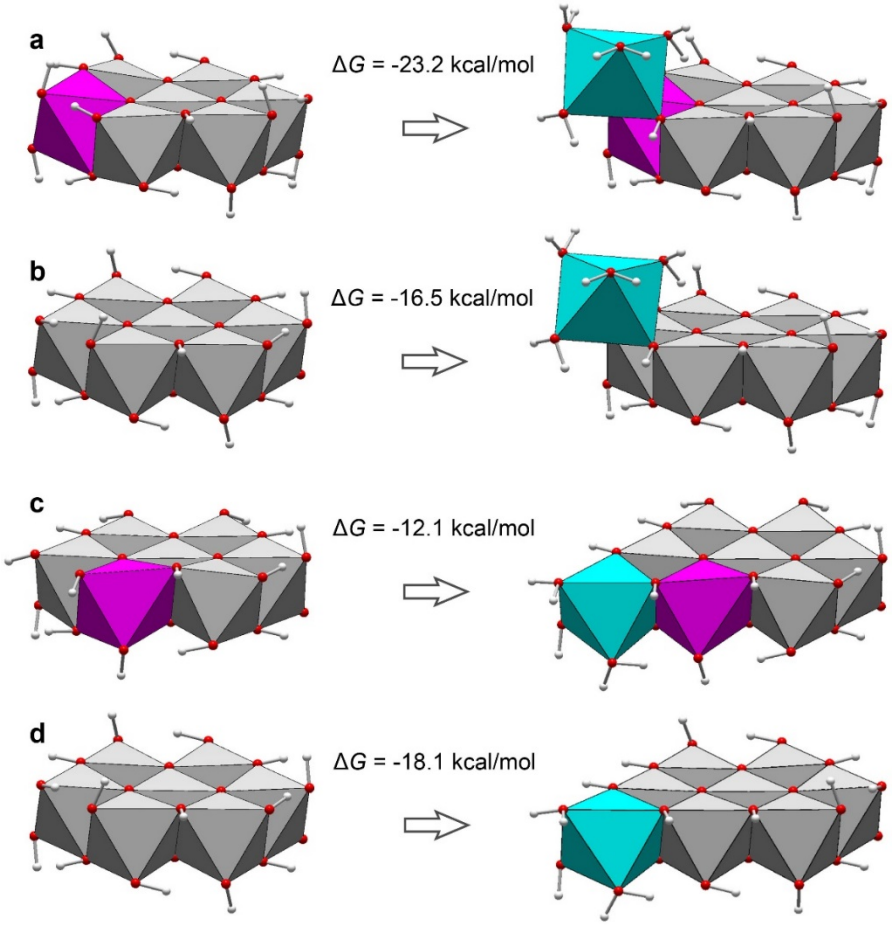

Figure S4. Schematic pathways and Gibbs free-energies of complexation (ΔG) of hexahydrated Co(II) as DCS (a, b) and DES (c, d) complex on the $Mn^{3+}Mn_6^{4+}$ (a, c) and Mn_7^{4+} (b, d) nanolayers. Mn(IV) octahedron = gray; Mn(III) octahedron = purple; Co(II) octahedron = cyan; oxygen = red, proton = gray.

Cartesian coordinates

$Mn_{TCS}^{3+\downarrow}Mn_{Layer}^{3+\uparrow}Mn_8^{4+}V$

25	0.467004000	2.659666000	-1.844696000
25	0.134271000	0.049651000	0.206529000
25	-0.399880000	-2.797242000	0.082806000
25	3.473410000	3.670588000	0.015906000
25	2.842050000	0.913590000	0.066682000
25	-2.283683000	1.815757000	0.030441000
25	-2.689708000	-0.991784000	-0.042118000
25	1.160178000	5.492775000	-0.057236000
25	2.393718000	-1.925394000	0.064646000
25	-1.667998000	4.695297000	-0.063163000
8	1.009162000	1.021354000	-2.939070000
8	1.554406000	3.748435000	-3.188691000
8	-1.188732000	2.991019000	-3.385320000
8	-1.974101000	-2.355782000	1.121174000
8	1.851784000	4.080058000	1.084352000
8	-4.292269000	-0.879697000	0.843281000
8	3.330455000	-0.658685000	1.167686000
8	-0.447821000	5.787202000	0.963804000

8	2.798880000	-3.369775000	1.105452000
8	-1.469404000	3.117759000	1.153366000
8	-1.321420000	-3.939467000	-1.002311000
8	2.432177000	2.419186000	-0.911542000
8	-3.071679000	0.532627000	-1.174830000
8	4.456752000	0.650759000	-0.957251000
8	0.653407000	6.786404000	-1.266593000
8	1.182868000	-2.956990000	-1.021529000
8	-2.613760000	3.406399000	-1.125292000
8	4.951930000	3.393333000	-0.980557000
8	1.328053000	1.136088000	1.096564000
8	-1.894731000	0.374262000	1.033989000
8	2.124433000	6.659232000	0.933455000
8	0.751531000	-1.588354000	1.031542000
8	-3.158316000	5.126482000	0.892049000
8	4.320885000	4.955630000	1.052397000
8	-0.960464000	-1.212606000	-0.817008000
8	2.690560000	5.036506000	-1.142305000
8	1.954777000	-0.321779000	-0.955417000
8	-1.972144000	6.063122000	-1.183330000
8	-0.608734000	1.545409000	-0.844728000
8	0.093487000	-4.180254000	1.222653000
8	-3.905517000	2.125188000	0.844675000
8	3.830145000	2.210065000	1.180470000
8	-3.429471000	-2.199273000	-1.246062000
8	3.886290000	-2.230756000	-0.959836000
8	-0.011553000	4.224751000	-0.929276000
1	-1.403145000	2.134255000	-3.773626000
1	-1.904864000	3.166616000	-2.739620000
1	0.964208000	4.320588000	-3.697757000
1	2.112831000	4.345771000	-2.638450000
1	1.713083000	1.262919000	-3.555581000
1	1.427694000	0.377752000	-2.283750000
1	-1.083554000	6.439739000	-1.374620000
1	0.838805000	6.431716000	-2.146449000
1	3.267647000	5.806716000	-1.240433000
1	4.949779000	2.421866000	-1.137253000
1	-0.337663000	5.431673000	1.857783000
1	2.974676000	6.211855000	1.133237000
1	5.160774000	5.182354000	0.637589000
1	-3.528129000	4.297112000	1.230871000
1	-3.775075000	2.052117000	1.798492000
1	-4.367148000	0.029654000	1.168964000
1	-3.162727000	-1.913985000	-2.128814000
1	-2.563910000	-3.118052000	1.198394000
1	-3.555571000	3.625567000	-1.137069000
1	0.042476000	-3.826837000	2.119382000
1	1.463919000	-3.879930000	-1.080980000
1	1.939871000	-3.792422000	1.301631000
1	4.219795000	-1.345435000	-1.189125000
1	4.277524000	-0.827929000	1.072021000
1	4.172271000	0.636462000	-1.878722000
1	4.776758000	2.012815000	1.175201000
1	-2.153108000	-3.468746000	-1.219999000
1	-4.032179000	0.652412000	-1.195992000
1	1.374555000	3.233204000	1.005407000
1	-0.543727000	2.860727000	1.261477000

$Co_{TCS}^{2+}Mn_9^{4+}V$

27	0.589774000	2.694016000	-1.994108000
25	0.071242000	-0.028425000	0.084311000

25	-0.423382000	-2.899183000	0.066526000
25	3.416126000	3.706640000	0.029173000
25	2.672260000	0.968531000	0.077302000
25	-2.132535000	1.709193000	0.032058000
25	-2.674433000	-1.091888000	0.011733000
25	1.130922000	5.573754000	-0.066007000
25	2.310088000	-1.914562000	0.095770000
25	-1.581635000	4.607486000	-0.020165000
8	1.197904000	1.005645000	-3.197617000
8	1.713848000	3.953099000	-3.344959000
8	-1.085144000	2.997646000	-3.331694000
8	-1.972724000	-2.488674000	1.129337000
8	1.857143000	4.199483000	1.121841000
8	-4.147769000	-0.840737000	1.052036000
8	3.166157000	-0.593546000	1.184145000
8	-0.462383000	5.802112000	0.993802000
8	2.770419000	-3.300152000	1.151783000
8	-1.233085000	2.951463000	1.123046000
8	-1.337673000	-4.054197000	-1.005258000
8	2.326036000	2.467570000	-0.889133000
8	-3.078312000	0.439118000	-1.081599000
8	4.216241000	0.616423000	-0.996147000
8	0.605404000	6.861648000	-1.273075000
8	1.171109000	-3.009431000	-1.005306000
8	-2.518789000	3.271067000	-1.071591000
8	4.884386000	3.376979000	-0.975002000
8	1.107864000	1.116419000	1.070535000
8	-1.603493000	0.221361000	0.998041000
8	2.107319000	6.789690000	0.906113000
8	0.635889000	-1.602380000	1.016794000
8	-3.079675000	4.895445000	1.018367000
8	4.340604000	4.917345000	1.065264000
8	-0.995730000	-1.349680000	-0.884637000
8	2.693165000	5.100539000	-1.117316000
8	1.671906000	-0.288666000	-0.888513000
8	-2.054930000	5.947311000	-1.124785000
8	-0.600343000	1.366683000	-0.949508000
8	0.152523000	-4.245514000	1.206740000
8	-3.691186000	1.972737000	1.037146000
8	3.686458000	2.199081000	1.180902000
8	-3.534344000	-2.270424000	-1.096712000
8	3.775901000	-2.096700000	-0.957338000
8	0.030170000	4.309472000	-0.907228000
1	-1.287615000	2.149571000	-3.744316000
1	-1.782973000	3.122087000	-2.653079000
1	1.089232000	4.558253000	-3.762767000
1	2.191584000	4.497682000	-2.683686000
1	2.034080000	1.229413000	-3.623749000
1	1.437092000	0.360512000	-2.494677000
1	-1.215389000	6.392636000	-1.357367000
1	0.677171000	6.454836000	-2.146915000
1	3.289176000	5.861813000	-1.156225000
1	4.860118000	2.415286000	-1.150458000
1	-0.315195000	5.460031000	1.887652000
1	2.930764000	6.344157000	1.170730000
1	5.211251000	5.045431000	0.671180000
1	-3.458124000	4.029871000	1.238842000
1	-3.430371000	2.021698000	1.965302000
1	-4.180132000	0.115792000	1.246097000
1	-3.374118000	-1.980683000	-2.004260000
1	-2.571361000	-3.247367000	1.174924000

1	-3.463429000	3.478827000	-1.082928000
1	-0.075391000	-3.976515000	2.105228000
1	1.497963000	-3.917117000	-1.066208000
1	1.923754000	-3.761583000	1.337182000
1	4.080280000	-1.175959000	-1.118719000
1	4.122160000	-0.736570000	1.162076000
1	3.932576000	0.762346000	-1.907549000
1	4.621300000	1.950786000	1.202037000
1	-2.172214000	-3.597937000	-1.225336000
1	-4.032564000	0.599947000	-1.051209000
1	1.319992000	3.397045000	1.085616000
1	-0.325397000	2.596860000	1.117616000

$Co_{INC}^{3+}Mn^{3+}Mn_{8}^{4+}$

27	0.592551000	2.861255000	0.012867000
25	0.015299000	0.029282000	0.004408000
25	-0.583434000	-2.850934000	0.076055000
25	3.309986000	3.805581000	-0.007936000
25	2.697109000	1.022054000	0.052342000
25	-2.083352000	1.881307000	0.035821000
25	-2.790481000	-0.965967000	0.021787000
25	1.107365000	5.653607000	-0.084884000
25	2.194630000	-1.854387000	0.070722000
25	-1.620336000	4.706990000	-0.063740000
8	-2.115068000	-2.385910000	1.166154000
8	1.670584000	4.154181000	0.916539000
8	-4.208688000	-0.567587000	1.124759000
8	3.081527000	-0.545793000	1.181586000
8	-0.491556000	5.883645000	0.977182000
8	2.628417000	-3.265257000	1.129862000
8	-1.063315000	3.130503000	0.948740000
8	-1.429806000	-4.186866000	-0.864715000
8	2.226366000	2.522643000	-0.933283000
8	-3.073362000	0.600602000	-1.082458000
8	4.251890000	0.688132000	-1.017074000
8	0.546620000	7.011087000	-1.241438000
8	1.024095000	-2.943370000	-1.021840000
8	-2.533010000	3.384815000	-1.121846000
8	4.798185000	3.516601000	-1.038721000
8	1.234556000	1.428236000	1.070093000
8	-1.639373000	0.327062000	0.950173000
8	2.081173000	6.811469000	0.958137000
8	0.509055000	-1.548380000	0.962046000
8	-3.103886000	4.975705000	0.990399000
8	4.195731000	5.011543000	1.073882000
8	-1.270953000	-1.473954000	-0.978777000
8	2.621701000	5.188498000	-1.178423000
8	1.692339000	-0.221898000	-0.902304000
8	-2.073690000	6.084809000	-1.165764000
8	-0.504788000	1.603826000	-0.940770000
8	0.006272000	-4.157474000	1.294835000
8	-3.609770000	2.198043000	1.101171000
8	3.728570000	2.298833000	1.119062000
8	-3.895455000	-2.050518000	-0.954667000
8	3.689069000	-2.085181000	-0.955249000
8	0.014408000	4.379491000	-0.994438000
1	-1.223344000	6.537645000	-1.348675000
1	0.755534000	6.724244000	-2.138249000
1	3.238151000	5.932936000	-1.210662000
1	4.815854000	2.554411000	-1.202050000
1	-0.343261000	5.503497000	1.854290000

1	2.907587000	6.335474000	1.170392000
1	5.053088000	5.201960000	0.676233000
1	-3.434078000	4.082497000	1.203381000
1	-3.321111000	2.143509000	2.020789000
1	-4.177068000	0.397988000	1.260324000
1	-3.350454000	-2.446501000	-1.644363000
1	-2.737910000	-3.125210000	1.170012000
1	-3.482436000	3.565959000	-1.095347000
1	-0.116321000	-3.786075000	2.176468000
1	1.348748000	-3.851032000	-1.085231000
1	1.771081000	-3.703414000	1.322899000
1	4.017294000	-1.179888000	-1.130206000
1	4.027984000	-0.740458000	1.197809000
1	3.968257000	0.744169000	-1.937342000
1	4.676553000	2.125771000	1.038814000
1	-1.691895000	-3.814030000	-1.714314000
1	-4.016289000	0.811214000	-1.108192000

$^{IV}Co_{TCS}^{2+}Mn_{9}^{4+}V$

27	0.402820000	2.784259000	-1.605758000
25	-0.027833000	-0.023488000	0.081381000
25	-0.516659000	-2.888613000	0.055342000
25	3.308553000	3.757261000	0.009290000
25	2.581709000	0.990949000	0.006671000
25	-2.244446000	1.725453000	0.145880000
25	-2.774366000	-1.083729000	0.095559000
25	1.029907000	5.662058000	0.057749000
25	2.215743000	-1.890141000	0.018123000
25	-1.702863000	4.637179000	0.157213000
8	-2.031140000	-2.495507000	1.166268000
8	1.779916000	4.201177000	1.144912000
8	-4.213955000	-0.870323000	1.187563000
8	3.091978000	-0.566066000	1.089719000
8	-0.547029000	5.812014000	1.166198000
8	2.704822000	-3.271886000	1.061856000
8	-1.265597000	2.935311000	1.208536000
8	-1.460027000	-4.030790000	-0.999464000
8	2.233755000	2.511951000	-0.956827000
8	-3.234611000	0.471332000	-0.944995000
8	4.100824000	0.651011000	-1.086578000
8	0.585836000	7.055015000	-1.018620000
8	1.050579000	-2.980853000	-1.056345000
8	-2.606664000	3.306067000	-0.909779000
8	4.762905000	3.476987000	-1.031565000
8	1.028734000	1.146976000	1.023837000
8	-1.672682000	0.215904000	1.060044000
8	2.042943000	6.785124000	1.086880000
8	0.564335000	-1.583602000	0.986285000
8	-3.122102000	4.834166000	1.292866000
8	4.249870000	4.927778000	1.065861000
8	-1.121263000	-1.327223000	-0.861671000
8	2.541921000	5.177668000	-1.060604000
8	1.549090000	-0.254141000	-0.939530000
8	-2.345546000	5.990524000	-0.844901000
8	-0.762058000	1.374162000	-0.929747000
8	0.101510000	-4.241183000	1.161629000
8	-3.752331000	1.986213000	1.210760000
8	3.614719000	2.210366000	1.103929000
8	-3.664848000	-2.247282000	-1.001911000
8	3.650618000	-2.067997000	-1.072894000
8	-0.137132000	4.498383000	-0.884984000

1	-1.738469000	6.089571000	-1.588808000
1	0.282076000	6.675131000	-1.852684000
1	3.145402000	5.932582000	-1.113793000
1	4.742855000	2.528884000	-1.259643000
1	-0.366619000	5.443517000	2.043025000
1	2.871941000	6.313463000	1.284953000
1	5.099767000	5.093641000	0.640737000
1	-3.514907000	3.954299000	1.426669000
1	-3.466101000	1.964419000	2.133099000
1	-4.247456000	0.073937000	1.424973000
1	-3.528744000	-1.948723000	-1.910494000
1	-2.627220000	-3.255141000	1.227668000
1	-3.549236000	3.516531000	-0.960487000
1	-0.122444000	-3.997817000	2.068577000
1	1.380075000	-3.886117000	-1.137899000
1	1.865423000	-3.740777000	1.263006000
1	3.951812000	-1.148377000	-1.242786000
1	4.048698000	-0.703179000	1.051693000
1	3.816494000	0.821443000	-1.993484000
1	4.551480000	1.968631000	1.088775000
1	-2.303942000	-3.576810000	-1.186105000
1	-4.187795000	0.621818000	-0.865829000
8	1.578105000	0.162438000	-3.648328000
8	1.869270000	5.030188000	-3.875517000
8	0.447356000	2.501515000	-3.609311000
1	0.883277000	1.600734000	-3.734763000
1	-0.435627000	2.437710000	-3.994413000
1	1.375469000	4.203075000	-3.974280000
1	2.086509000	5.055663000	-2.929420000
1	2.504939000	0.228639000	-3.903616000
1	1.592664000	-0.031278000	-2.684282000
1	1.246246000	3.399496000	1.195756000
1	-0.369739000	2.548461000	1.218204000

$^{IV}Co_{TCS}^{2+}Mn_9^{4+}V_d$

27	0.425868000	2.811349000	-1.497408000
25	0.004361000	-0.029843000	0.064106000
25	-0.523465000	-2.892140000	0.050737000
25	3.166085000	3.772055000	0.057210000
25	2.621600000	0.948886000	-0.011315000
25	-2.161981000	1.807968000	0.173177000
25	-2.740001000	-1.032799000	0.162240000
25	0.994207000	5.625216000	0.024285000
25	2.222349000	-1.931396000	-0.036820000
25	-1.760553000	4.618210000	0.079907000
8	-1.983509000	-2.474624000	1.221485000
8	1.624157000	4.164422000	0.956300000
8	-4.131277000	-0.763910000	1.306937000
8	3.144889000	-0.649201000	1.047772000
8	-0.598227000	5.766177000	1.131183000
8	2.712356000	-3.350885000	0.974013000
8	-1.267267000	3.066897000	1.039885000
8	-1.535155000	-4.011712000	-0.979670000
8	2.276030000	2.440309000	-1.012052000
8	-3.222179000	0.455315000	-0.903789000
8	4.178605000	0.601277000	-1.066389000
8	0.548968000	7.113990000	-1.044713000
8	1.022263000	-3.008092000	-1.102958000
8	-2.666026000	3.273704000	-0.994246000
8	4.748940000	3.546503000	-0.934702000
8	1.104517000	1.052986000	1.013849000

8	-1.589697000	0.248877000	1.081252000
8	1.986514000	6.773866000	1.083726000
8	0.598389000	-1.624640000	0.959725000
8	-3.243618000	4.865232000	1.167982000
8	4.105460000	4.934159000	1.161756000
8	-1.125563000	-1.336027000	-0.850793000
8	2.518638000	5.179107000	-1.108744000
8	1.585394000	-0.299678000	-0.976257000
8	-2.401465000	6.045450000	-0.923069000
8	-0.725550000	1.350679000	-0.956204000
8	0.096559000	-4.282073000	1.125887000
8	-3.688551000	1.980427000	1.279876000
8	3.540387000	2.204280000	1.144920000
8	-3.697537000	-2.223768000	-0.875323000
8	3.648825000	-2.110753000	-1.151970000
8	-0.211320000	4.564039000	-1.028049000
1	-1.694885000	6.263707000	-1.540280000
1	0.263851000	6.749832000	-1.889789000
1	3.139681000	5.920119000	-1.112982000
1	4.777867000	2.610937000	-1.182424000
1	-0.404609000	5.322691000	1.968653000
1	2.786333000	6.266898000	1.313721000
1	4.987314000	4.997274000	0.776429000
1	-3.527838000	3.973504000	1.424166000
1	-3.360881000	2.093170000	2.180377000
1	-4.120579000	0.200238000	1.487073000
1	-3.709390000	-1.869613000	-1.772922000
1	-2.591268000	-3.223468000	1.288533000
1	-3.617873000	3.437628000	-0.959211000
1	-0.093078000	-4.039317000	2.040375000
1	1.341231000	-3.918084000	-1.169574000
1	1.867559000	-3.802532000	1.188797000
1	3.958169000	-1.189849000	-1.302596000
1	4.096011000	-0.799464000	0.961345000
1	3.959463000	0.887128000	-1.960956000
1	4.494821000	2.051954000	1.109197000
1	-2.366271000	-3.520182000	-1.135135000
1	-4.170677000	0.606472000	-0.795664000
8	1.673903000	0.209460000	-3.636979000
8	1.944375000	4.969737000	-3.881782000
8	0.473861000	2.532530000	-3.542540000
1	0.930232000	1.647029000	-3.672217000
1	-0.412771000	2.439797000	-3.911401000
1	1.423920000	4.153240000	-3.936099000
1	2.141949000	5.044324000	-2.931528000
1	2.605462000	0.339666000	-3.845927000
1	1.660027000	-0.015177000	-2.676513000

$Co_{INC}^{2+,LS}Mn_9^{4+}$

27	0.497412000	2.776377000	0.032402000
25	0.017359000	0.027115000	0.007764000
25	-0.509008000	-2.829111000	-0.035663000
25	3.260633000	3.742176000	-0.031120000
25	2.729731000	0.964733000	-0.074550000
25	-2.216768000	1.845811000	0.133727000
25	-2.726958000	-0.986706000	0.007674000
25	0.992271000	5.524265000	0.003354000
25	2.236694000	-1.894845000	-0.032487000
25	-1.764916000	4.642620000	0.096782000
8	-2.014965000	-2.429347000	1.075822000
8	1.636467000	4.000178000	0.916790000

8	-4.167239000	-0.760626000	1.083604000
8	3.121090000	-0.609972000	1.069878000
8	-0.564249000	5.759017000	1.125193000
8	2.680591000	-3.307103000	1.009080000
8	-1.439186000	3.086147000	1.164997000
8	-1.475229000	-3.932687000	-1.113038000
8	2.440599000	2.421981000	-1.091340000
8	-3.123753000	0.524066000	-1.063391000
8	4.274042000	0.500919000	-1.028975000
8	0.422323000	6.908239000	-1.130832000
8	1.064260000	-2.958689000	-1.132256000
8	-2.717646000	3.344003000	-0.987725000
8	4.844557000	3.700404000	-0.988466000
8	1.132629000	1.221144000	0.927845000
8	-1.609694000	0.272055000	0.998539000
8	1.990719000	6.680291000	1.032465000
8	0.581127000	-1.550515000	0.917911000
8	-3.250086000	5.080415000	1.128981000
8	4.086210000	4.945741000	1.131286000
8	-1.060626000	-1.238855000	-0.949486000
8	2.480719000	5.108505000	-1.160334000
8	1.627686000	-0.266739000	-0.993387000
8	-2.189609000	6.035868000	-1.017396000
8	-0.629348000	1.557258000	-0.881979000
8	0.061019000	-4.210844000	1.060656000
8	-3.828935000	1.898980000	1.078514000
8	3.692222000	2.203479000	1.067669000
8	-3.614737000	-2.163945000	-1.102416000
8	3.684310000	-2.119891000	-1.101394000
8	-0.161794000	4.290154000	-0.864518000
1	-1.332087000	6.474617000	-1.199129000
1	0.567271000	6.593348000	-2.031611000
1	3.069391000	5.871440000	-1.236724000
1	4.677955000	3.187970000	-1.787621000
1	-0.396282000	5.362317000	1.990976000
1	2.824860000	6.197675000	1.211877000
1	4.916056000	5.212145000	0.719522000
1	-3.246298000	4.477974000	1.880708000
1	-3.657705000	2.334738000	1.920191000
1	-4.174053000	0.205873000	1.280009000
1	-3.588336000	-1.792342000	-1.992868000
1	-2.621854000	-3.181412000	1.113156000
1	-3.663900000	3.502528000	-0.864304000
1	-0.192387000	-3.983501000	1.963773000
1	1.374772000	-3.871524000	-1.200657000
1	1.827206000	-3.753701000	1.196924000
1	4.005013000	-1.204363000	-1.275736000
1	4.070477000	-0.791098000	1.072087000
1	4.261291000	1.001549000	-1.852291000
1	4.639659000	2.034888000	0.968891000
1	-2.303879000	-3.442776000	-1.295287000
1	-4.078853000	0.674210000	-1.062349000
8	1.945140000	0.156786000	-3.672590000
8	1.421176000	4.333720000	-3.756439000
8	-0.132294000	2.036974000	-3.515319000
1	0.575435000	1.377632000	-3.660814000
1	-0.369480000	1.902897000	-2.571538000
1	0.857269000	3.545015000	-3.610913000
1	1.751134000	4.566564000	-2.874625000
1	2.703755000	0.750480000	-3.692841000
1	1.837952000	-0.053196000	-2.718757000